JWST observations of the Ring Nebula (NGC 6720): I. Imaging of the rings, globules, and arcs

(article starts on next page)

JWST observations of the Ring Nebula (NGC 6720): I. Imaging of the rings, globules, and arcs

R. Wesson [1,2]★ Mikako Matsuura [1] Albert A. Zijlstra,[3] Kevin Volk,[4] Patrick J. Kavanagh [5,6]
Guillermo García-Segura,[7] I. McDonald [3,8] Raghvendra Sahai,[9] M. J. Barlow [2] Nick L. J. Cox,[10]
Jeronimo Bernard-Salas,[10,11] Isabel Aleman [12,13] Jan Cami [14,15,16] Nicholas Clark,[14,15] Harriet
L. Dinerstein,[17] K. Justtanont,[18] Kyle F. Kaplan,[17] A. Manchado,[19,20,21] Els Peeters [14,15,16] Griet C. Van
de Steene[22] and Peter A. M. van Hoof[22]

Affiliations are listed at the end of the paper

ABSTRACT
We present *JWST* images of the well-known planetary nebula NGC 6720 (the Ring Nebula), covering wavelengths from 1.6 to 25 μm. The bright shell is strongly fragmented with some 20 000 dense globules, bright in H_2, with a characteristic diameter of 0.2 arcsec and density $n_H \sim 10^5$–10^6 cm^{-3}. The shell contains a narrow ring of polycyclic aromatic hydrocarbon (PAH) emission. H_2 is found throughout the shell and also in the halo. H_2 in the halo may be located on the swept-up walls of a biconal polar flow. The central cavity is filled with high-ionization gas and shows two linear structures which we suggest are the edges of a biconal flow, seen in projection against the cavity. The central star is located 2 arcsec from the emission centroid of the cavity and shell. Linear features ('spikes') extend outward from the ring, pointing away from the central star. Hydrodynamical simulations reproduce the clumping and possibly the spikes. Around 10 low-contrast, regularly spaced concentric arc-like features are present; they suggest orbital modulation by a low-mass companion with a period of about 280 yr. A previously known much wider companion is located at a projected separation of about 15 000 au; we show that it is an M2–M4 dwarf. NGC 6720 is therefore a triple star system. These features, including the multiplicity, are similar to those seen in the Southern Ring Nebula (NGC 3132) and may be a common aspect of such nebulae.

Key words: planetary nebulae: general – planetary nebulae: individual: NGC6720 – circumstellar matter – stars: evolution.

1 INTRODUCTION

Planetary nebulae (PNe) are composed of the ionized ejecta from low- to intermediate-mass stars ($<8\,M_\odot$) at the ends of their lives. PNe can be used as astrophysical laboratories, having a single exciting central star and hosting a range of ionized, neutral, and molecular lines as well as dust emission. They are ideal objects to study the physics and chemistry of gaseous media under well-defined conditions. The structures shown by PNe range from their global shape to compact condensations, including filaments and globules. They can be used to study the hydrodynamical origin of such features. Specific questions that can be studied using PNe include the formation and destruction of molecules including H_2 and polycyclic aromatic hydrocarbons (PAHs), and the role of stellar interactions in the shaping of the nebulae.

We report here on *JWST* imaging of the Ring Nebula, NGC 6720, using 13 filters from 1.6 to 25 μm. The different filters trace a range of emission lines and dust features. *JWST*'s high angular resolution enables us to trace the ionized, molecular, and dust components of the nebula. Due to its proximity, high-angular resolution and

high-sensitivity JWST images can reveal details of the physics and chemistry in small structures such as globules and filaments in this PN. These features are shared with the Southern Ring Nebula (NGC 3132), which was also imaged by JWST (De Marco et al. 2022).

This paper is one of four describing new *JWST* observations of the Ring Nebula, together with a study of the central star and its close environs (Sahai et al. in preparation), a study of the rich H_2 emission line spectra in two subregions of the nebula (van Hoof et al. in preparation), and a study of the PAH emission in two subregions of the nebula (Clark et al., in preparation).

2 BASIC PROPERTIES OF THE RING NEBULA

The Ring Nebula (NGC 6720 or M 57) is located at a distance of 790 ± 30 pc, as derived from the *Gaia* parallax of the central star of 1.2696 ± 0.0438 mas (Lindegren et al. 2021). It has a visual diameter of about 4 arcmin (equivalent to $\sim 2 \times 10^5$ au or ~ 1 pc) and shows a complex morphology (O'Dell et al. 2013a). The distance puts the central star 190 pc above the Galactic plane, consistent with membership of the thin disc.

HST narrow-band images at a variety of optical wavelengths (O'Dell, McCullough & Meixner 2004; O'Dell, Sabbadin & Henney 2007; O'Dell et al. 2013a) have been used to derive plasma param-

★ E-mail: rw@nebulousresearch.org

Table 1. Observing log.

Instrument	Filter	λ_p (μm)	BW (μm)	PSF ($''$)	t_{exp} (sec)	F_{tot} (Jy)	North Spec contributions Cont	H I	H$_2$	Others	Notes
NIRCam	F162M	1.626	0.168	0.053	1933	0.113 ± 0.017	81 per cent	10 per cent	4 per cent	He I (1 per cent)	
	F212N	2.121	0.027	0.069	1933	0.9 ± 0.08	13 per cent		85 per cent		
	F300M	2.996	0.318	0.097	483	0.1511 ± 0.0002	58 per cent	10 per cent	27 per cent	He II (1 per cent)	
	F335M	3.365	0.347	0.109	483	0.2124 ± 0.0003	53 per cent	6 per cent	37 per cent		PAHs
MIRI	F560W	5.6	1.2	0.207	444	0.44 ± 0.02	62 per cent	2 per cent	32 per cent		
	F770W	7.7	2.2	0.269	444	0.816 ± 0.01	68 per cent	5 per cent	14 per cent	[Ar II] (9 per cent)	PAHs
	F1000W	10.0	2.0	0.328	444	1.86 ± 0.02	46 per cent		11 per cent	[S IV] (26 per cent); [Ar III] (14 per cent)	
	F1130W	11.3	0.7	0.375	444	0.7253 ± 0.003	94 per cent			[Ni I] (3 per cent)	PAHs
	F1280W	12.8	2.4	0.420	444	1.20 ± 0.02	45 per cent	2 per cent	1 per cent	[Ne II] (49 per cent)	
	F1500W	15.0	3.0	0.488	444	7.43 ± 0.02	4 per cent			[Ne III] (94 per cent)	
	F1800W	18.0	3.0	0.591	444	4.01 ± 0.02	42 per cent			[S III] (54 per cent)	
	F2100W	21.0	5.0	0.674	444	5.57 ± 0.03	71 per cent			[S III] (25 per cent); [Ar III] (1 per cent)	
	F2550W	25.5	4.0	0.803	444	20 ± 2	88 per cent			[O IV] (8 per cent)	
MIRI simul	F770W				951						
	F1130W				951						
	F1000W				951						

Note. λ_p: pivot wavelength in μm (NIRCam: Rieke et al. 2023; MIRI: Bouchet et al. 2015). BW: band width in μm. PSF: FWHMs of PSFs in arcsec. For NIRCam simulated values are taken. t_{exp}: exposure time on source in sec. F_{tot}: photon-weighted mean flux density (Bohlin, Gordon & Tremblay 2014) of the nebula in Jy (subsection 3.3). North Spec contributions: Estimated contributions to the images in each filter, calculated using NIRSpec-IFU and MIRI-MRS observations of a region in the northern part of the bright ring (Appendix Fig. C3; van Hoof et al. in preparation). Note that some filters are designated to detect specific PAH features, though these PAH bands are not the strongest contributors to the in-band flux in the North spectrum. The PAH spectra observed in the MIRI MRS spectra are discussed by Clark et al. (in preparation)

eters and extinction maps for the nebula (Ueta & Otsuka 2021). They find an extinction $c_{H\beta} = 0.2$, increasing to 0.4 in the shell.[1] The interstellar foreground extinction contributes $c_{H\beta} = 0.1$; the remainder of the extinction is internal to the circumstellar shell. The extinction is highest in micro-structures (clumps) in the shell (Ueta & Otsuka 2021).

The star currently has a temperature of $T_{eff} = 1.35 \times 10^5$ K and a luminosity of $L \approx 310\,L_{\odot}$ (Sahai et al, in preparation) which places it on the white dwarf cooling track. The current mass and progenitor mass of the central star are difficult to determine for objects on the cooling track, as the tracks tend to converge in that region of the HR diagram. González-Santamaría et al. (2021) quote $0.58\,M_{\odot}$ and $1.5\,M_{\odot}$, respectively, while the models of Miller Bertolami (2016) for the current temperature and luminosity are also consistent with a progenitor mass close to $2\,M_{\odot}$.

A post-AGB star of these masses reaches peak temperature at a luminosity $L \sim 3000\,L_{\odot}$. From this point, the luminosity declines to $\sim 200\,L_{\odot}$ within a few hundred years, before the decline slows down (Miller Bertolami 2016). The stellar luminosity of NGC 6720 ($L \approx 310\,L_{\odot}$) indicates that the star is currently in this phase of rapid fading. Part of the ionized nebula is likely recombining.

3 OBSERVATIONS AND DATA REDUCTION

3.1 *JWST* observations

The Ring Nebula was observed with *JWST* (Gardner et al. 2023) in Cycle 1 General Observers (GO) programme 1558. The observations were carried out in July and August 2022, using both NIRCam (Rieke et al. 2023) and MIRI (Wright et al. 2023).

The NIRCam observations were obtained on 2022 August 4. Four filters were used, with two filters for each of the Short Wavelength Camera (F162M and F212N) and the Long Wavelength Camera (F300M and F335M). The nebula was covered by a single field of view (FOV) with a 4-point dither pattern yielding a FOV of 2.45 arcmin with some gaps near the edges of the fields which depend on the camera. The field centre is at 18:53:35.079, +33:01:45.03 (J2000). The observing log is summarized in Table 1. NIRCam images of individual filter bands are shown in Appendix Fig. A1.

Imaging observations with MIRI were carried out on 2022 August 20, using nine filters. The exposure time was 444 s in each filter. The nebula was covered by a 1×2 mosaic with a 4-point dither pattern. The field size was 2.35×1.9 arcmin, again centred at 18:53:35.079, +33:01:45.03 (J2000).

Additionally, MIRI images in three filters (F770W, F1130W, and F1000W) were obtained in simultaneous imaging mode during separate MIRI MRS observations on 2022 July 4. These images are centred on 18:53:34.510, +33:02:09.11, which allows for some overlap with the direct MIRI images. The simultaneous observations capture part of the outer regions of the Ring Nebula. Their exposure time was 951 s per filter, hence these simultaneous observations have better sensitivities than those for the main field.

The pixel scales of the reduced data are 0.031 arcsec per pixel for the NIRCam short-wavelength camera images, 0.063 s for the NIRCam long-wavelength camera images, and 0.111 arcsec for the MIRI images.

3.2 Data reduction

The NIRCam imaging exposures were reduced using the *JWST* Calibration Pipeline[2] (Bushouse et al. 2022) version 1.9.6 with CRDS version 11.16.19 and CRDS context 'jwst_1075.pmap'. Each of

---

[1]We use the relation $c_{H\beta} = 1.46\,E(B - V)$.

[2]Available at https://github.com/spacetelescope/jwst

the NIRCam short- and long-wavelength exposures were processed through the `Detector1Pipeline` with the default parameters. At this point the ramp slope `_rate.fits` images had some of the 1/*f* noise removed using a standalone python code provided by Chris Willott outside of the pipeline[3] before going on to the subsequent data-reduction steps. The files were then processed through the `Image2Pipeline` and `Image3Pipeline` stages with the default parameters for all steps, except that the `tweakreg` step was called with the option to align the images to *Ga ia* Data Release 2[4] stars in the field. The *JWST* pipeline did not have the capability to align to *Ga ia* Data Release 3 at the time of the reduction of the images. The difference in the astrometry between using *JWST* Data Release 2 or *Gaia* Data Release 3 as the reference is expected to be 10 mas or less, based on comparison of the two catalogues and on a test of this option in pipeline version 1.11.1 on a different data set. For each of the four filters this resulted in a combined, resampled image that was used for the subsequent analysis.

It was observed that the 1/*f* noise removal interacted with the `Image3Pipeline skymatch` step to produce a low-level artefact in the short-wavelength images, in the regions to the left and right of the main nebula that are observed in 3 of the 9 mosaic positions. It is not clear why this happens in the `skymatch` step, since direct examination of the images before and after the 1/*f* noise removal does not show any obvious sign of an offset in the sky background level. This artefact is seen in the ratio image (see Fig. 11).

We processed all MIRI imaging exposures using *JWST* Calibration Pipeline version 1.8.3 with CRDS version 11.16.16 and context 'jwst_1062.pmap'. Each of the raw MIRI files was processed through `Detector1Pipeline` with default parameters. The world coordinate system (WCS) in pipeline-processed *JWST* data can often be incorrect, resulting from uncertainties in the pointing information that are introduced by guide star catalogue errors and roll uncertainty (see Pontoppidan et al. 2022). We corrected the WCS reference keywords in the `Detector1Pipeline` output by determining and applying the median offset between point sources in preliminary, fully calibrated exposures to their *Gaia* Data Release 3[5] counterparts. We then processed the resulting files through `Image2Pipeline` to create calibrated dither images across all filters. We created combined mosaics for each MIRI filter, which include the simultaneous imaging field for F770W, F1130W, and F1000W, using `Image3Pipeline`.

MIRI colour images were created by combining multiple filters, where the angular resolutions were matched. For each pair of images, we convolved the images using simulated PSFs, calculated using WebbPSF (Perrin et al. 2014). The convolution was processed using the PYTHON code PSF MATCHING (Gordon et al. 2008; Aniano et al. 2011).

3.3 Photon-weighted mean flux densities

Table 1 lists the photon-weighted mean flux densities (F_{tot} in Jy) of the main body (the bright shell) of the Ring Nebula. An elliptical aperture was placed centred on the central star. The major and minor radii of the elliptical aperture are 48 and 38 arcsec, respectively, and the rotation angle is 32° clockwise from north, aligned with the major axis of the nebula. The background flux level was estimated from apertures at two areas having the lowest backgrounds within the image (RA=18:53:30.225, Dec.= +33:01:55.80, and

[3] https://github.com/chriswillott/jwst

[4] https://www.cosmos.esa.int/web/gaia/dr2

[5] https://www.cosmos.esa.int/web/gaia/dr3

RA=18:53:40.480, Dec. = +33:02:03.91 (J2000), with a width of 8 arcsec and height of 4 arcsec and 140.52° as the NIRCam tilt angle). These apertures are shown in Appendix Fig. C4. The difference between these two background apertures is taken as an estimate of the uncertainty in the total flux. These uncertainties represent a systematic error (background subtraction) and not Poisson noise.

The flux in each filter includes emission lines and bands, bound-free and free–free continuum, and dust emission. The important contributions to each filter are listed in Table 1, based on NIRSPEC and MRS observations of a region in the northern part of the bright ring (Appendix Fig. C3; van Hoof et al. in preparation). The relative contributions will vary across the nebula.

4 DESCRIPTION AND ANALYSIS OF THE IMAGES

4.1 Stratification

The nebula can be divided into three clearly distinct regions: the central cavity, the bright shell and the halo. (The latter is sometimes divided into an inner and an outer halo; Balick et al. 1992). This structure can be recognized in the multicolour images of Fig. 1 (NIRCam) and Fig. 2 (MIRI). The components are labelled in Fig. 3. In these images, the regions show different colours. This indicates that they differ in their line emission: the nebula is stratified.

The low density central cavity appears as an approximately circular structure, with a radius of about 25 arcsec, which emits mainly in the F1000W and F2550W filters (Figs 4 and 5). These two filters contain the high-excitation [S IV] (ionization potential of 35 eV) and [O IV] (55 eV) lines (Table 1). All other filters show the cavity as a low-emission region (Figs 1, 2, 4, and Appendix A1). The cavity thus has a higher excitation than the surrounding nebula.

The cavity contains a linear structure approximately along the major axis of the nebula. The structure is visible in most filters and consists of two brighter stripes on either side of the central star. The region between these stripes shows little emission in any filters except for F2550W. The long-wavelength F1800W and F2100W filters do not show the stripes. A somewhat similar structure is present in the central region of NGC 3132 (De Marco et al. 2022), although there are also notable differences. O'Dell et al. (2013a) interpret the stripes in NGC 6720 as features in the inner halo, seen in projection against the cavity.

The shell surrounding the cavity is a broad region with a well defined inner and outer edge. It is bright in all filters. Unlike the central region, it has an elliptical shape. The outer radius is 44 arcsec along the major axis and 35 arcsec along the minor axis. The position angle of the major axis is 132° (from north to west). The shell is significantly brighter along the minor axis than the major axis.

The outer edge of the shell is somewhat distorted towards the north-east. This is approximately the direction of the *Gaia* DR3 proper motion of the central star (NNE, 10 km s^{-1}), and it is possible that this distortion is related to interaction with the interstellar medium.

The emission in the shell is clumpy, especially in filters dominated by H$_2$ (Table 1). The H$_2$ emission from the shell has long been known (Greenhouse, Hayward & Thronson 1988), and was known to be clumpy (Speck et al. 2003), but is seen at much higher angular resolution and sensitivity with *JWST*. Close inspection shows evidence for a very large number of clumps or globules, seen throughout the shell. The almost complete lack of clumps seen projected on the central cavity supports the interpretation of the shell as an equatorial or toroidal structure, seen approximately pole-on (Bryce, Balick & Meaburn 1994; O'Dell et al. 2013a).
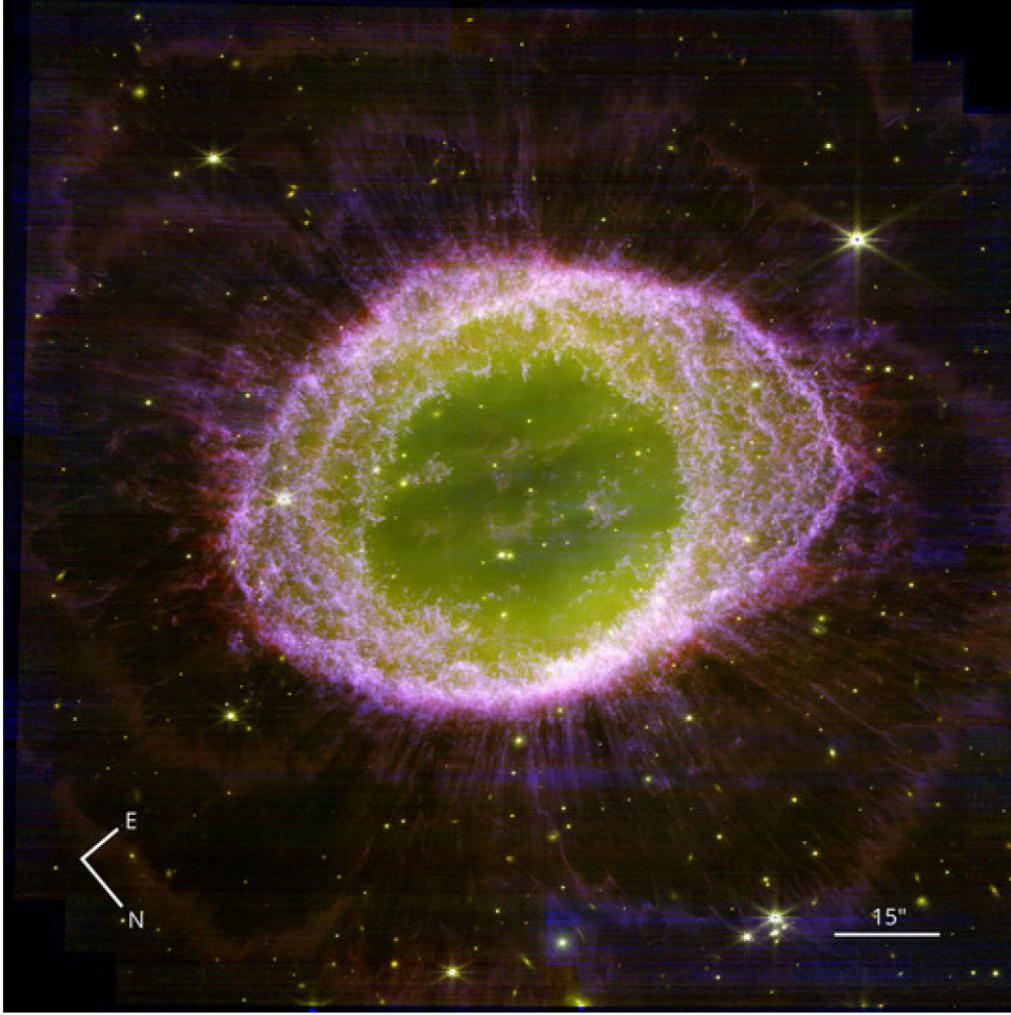
Figure 1. NIRCam three colour image: F212N (blue), F300M (green), and F335M (red). This is produced from the pipeline level3 products which does not include the 1/*f* noise removal step. Directions of north and east are indicated.

The inner halo is seen in all NIRCam images apart from F162M (Appendix Fig. A1). The inner halo is also seen in the MIRI F560W and F770W MIRI images; the filters that clearly show the halo are dominated by H_2 lines. H_2 emission from the halo was detected by van Hoof et al. (2010). The faint halo shows a wealth of structure, including concentric arcs, radial spikes, and distorted bright edges. These are each discussed separately in the following sections. The simultaneous fields show a part of the outer halo, terminating at a radius of 1.9 arcmin from the centre. The incomplete coverage of these fields shows structure consistent with a generally circular outer halo.

The central star is clearly detected in the NIRCam images and in the MIRI F560W and F770W images. The central star and its vicinity will be discussed in a separate paper (Sahai et al., in preparation).

4.2 Offset of the nebular centre from the stellar position

Although the outer edge of the inner cavity is close to circular, its centre does not exactly correspond to the position of the central star, but instead appears to be offset to the north-west (roughly in the direction of the *Gaia* companion; see subsection 5.2) by about 2 arcsec (Fig. 6). The flux-weighted centres of the F300M and F335M images (calculated as the first moment of the images) are also offset

from the central star, and nearly coincide with the centre of the inner cavity. The coordinates of the flux-weighted centre for the F300M image are RA=18:53:35.04 and Dec.=+33:01:46.8, while the coordinates of the centre of the circular inner edge of the cavity are RA=18:53:35.01, Dec. = +33:01:46.01.

This offset with the shell and cavity must be considered tentative, as the complex small scale structures introduce uncertainties. The interpretation is also open to discussion. The structures here are affected by the original mass-loss, the ionization, and the hot stellar wind. If the offset is interpreted as caused by the original mass-loss, for an age of 4000 yr (O'Dell et al. 2013b), the offset would correspond to a velocity difference between star and nebula of around $2\,\mathrm{km\,s^{-1}}$.

Off-centre central stars are known in some other PNe. The PN A39 has an offset of 2 arcsec in a symmetric nebula (Jacoby, Ferland & Korista 2001). Another example is Hu 2-1 (Miranda et al. 2001).

4.3 Globules

Fig. 7 shows a sequence of images of regions containing globules, covering optical (*HST*) and near- and mid-infrared (*JWST*) wavelengths. The *HST* images show the globules as extinction peaks (e.g. O'Dell et al. 2013a), while the *JWST* images do not. Even the
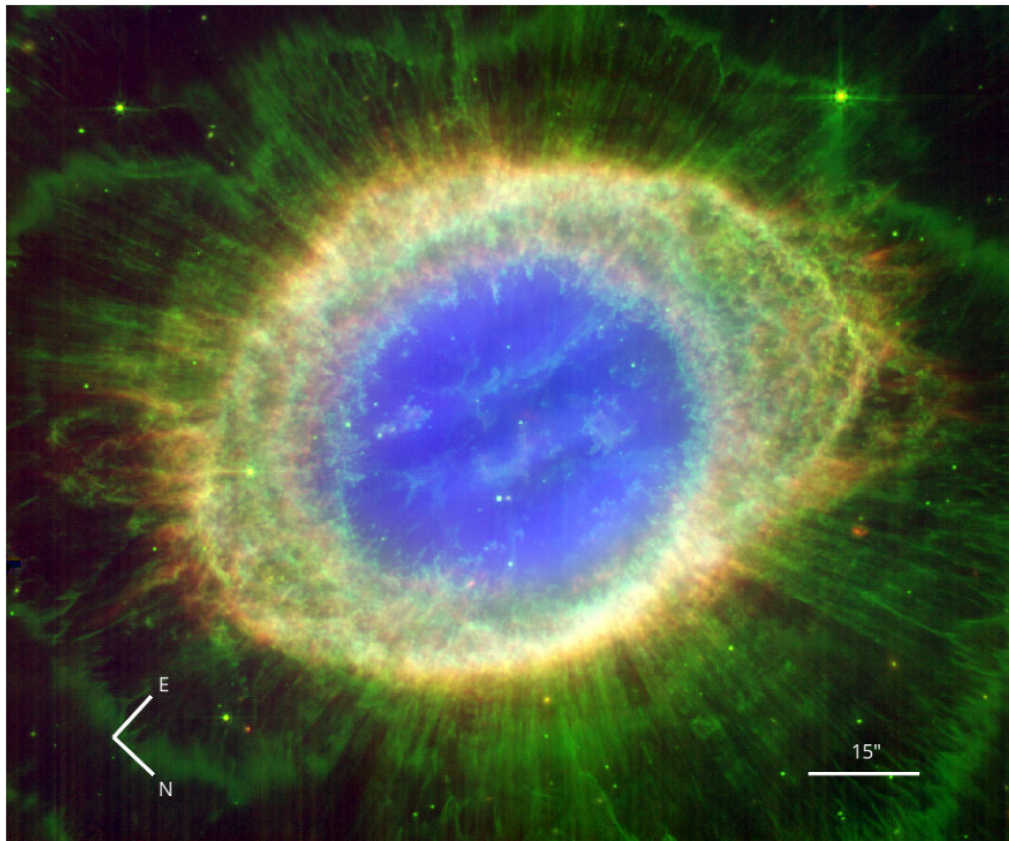
Figure 2. MIRI three-colour image: F2550W (blue), F560W (green), and F1130W (red). Directions of north and east are indicated.
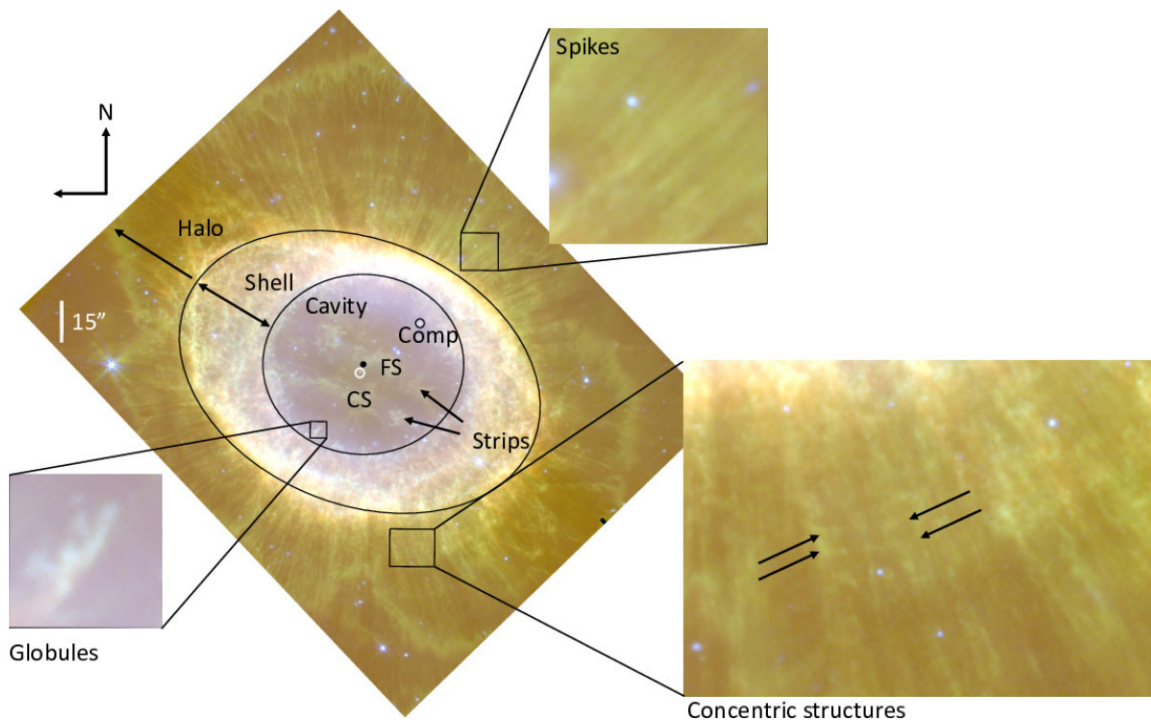
Figure 3. The names of the nebula components superposed on the NIRCam and MIRI three-colour image: F300M (blue), F560W (green), and F770W (red). CS (the white circle) is the central star, FS (black spot) is the first-moment centroid of the flux in the F300M image, and Comp is the companion star candidate. North is at the top in this image. The locations of some low-contrast concentric features are indicated, but they are much more easily seen in Fig. 9.
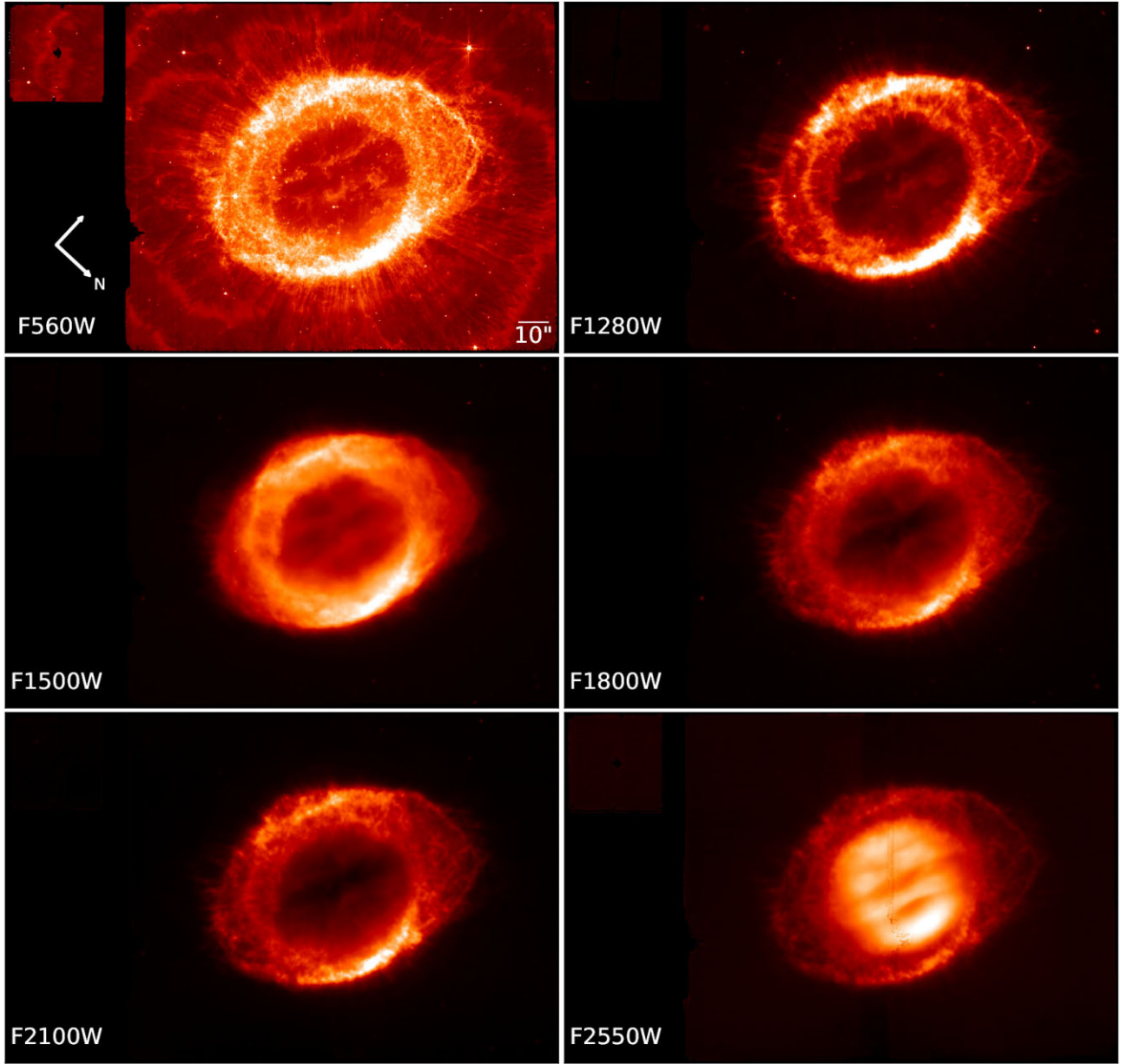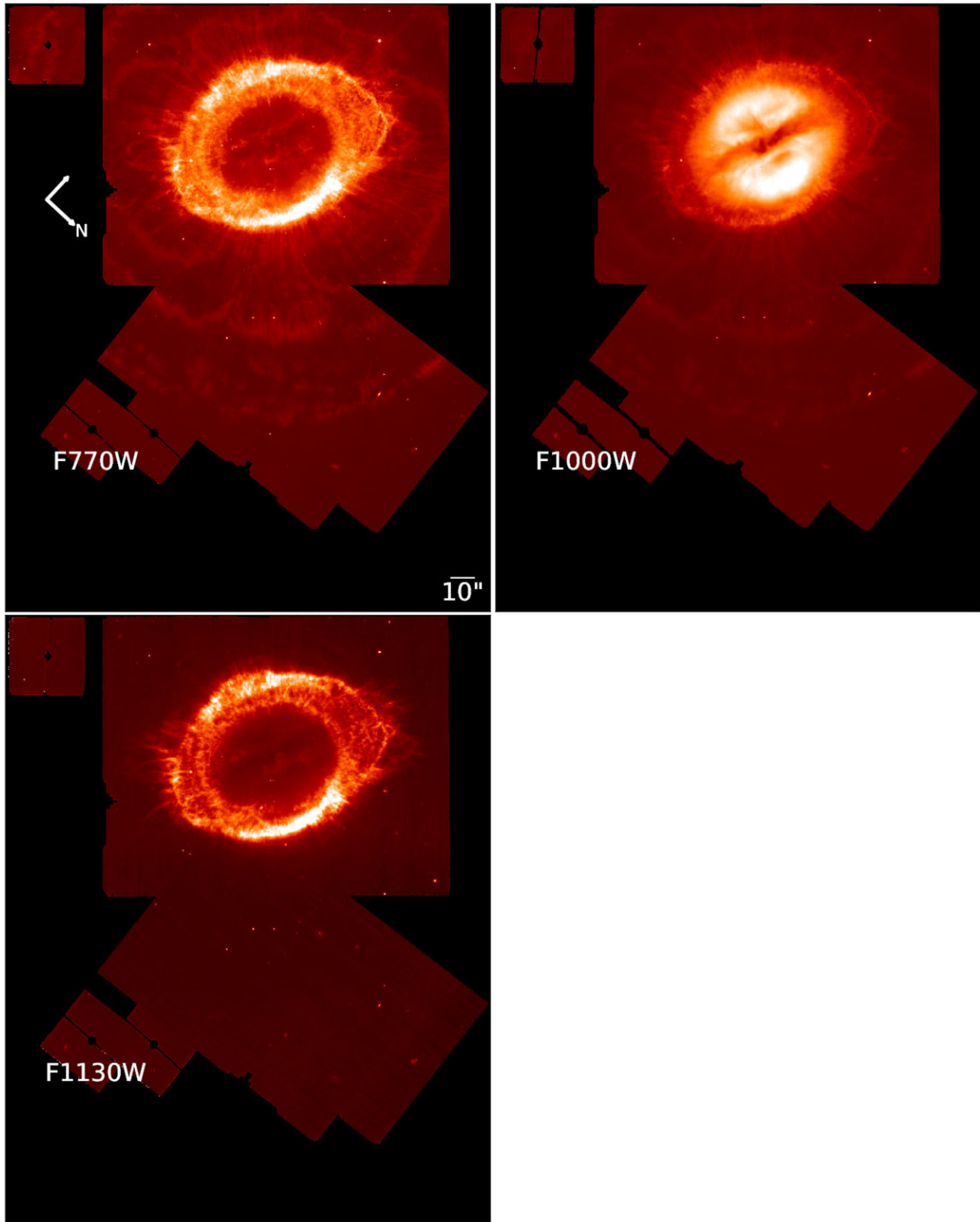
Figure 4. MIRI images of the Ring Nebula.

shortest wavelength NIRCam image at 1.62 μm shows no absorption (Appendix Fig. A1). This is in contrast to NGC 3132, in which De Marco et al. (2022) found some globules showing absorption at 1.87 μm. We note that the sensitivity to absorption is less in our data because of the choice of filters: the F187N filter used for NGC 3132 contains a strong HI Paα line, while the F162M and F212N filter do not contain strong atomic emission lines (Table 1). There is less absorbable nebular background in our images.

To estimate the mass of the globules in NGC 3132, De Marco et al. (2022) assumed $A_V = 1.7$ mag and 3.9 mag for two specific knots. We follow their analysis. A direct measurement of the most heavily extinguished globule in Fig. 7b gave an extinction $A_{502nm} = 1.1$ mag. Using the wavelength dependence of the extinction curve from Cardelli, Clayton & Mathis (1989), and $N(H)/A(V) \sim 2.3 \times 10^{21}$ cm^{-2}, the column density becomes $N_H \approx 2.5 \times 10^{21}$ cm^{-2}. The diameter of this

globule is about 0.4 arcsec. This yields a density $n_H \approx 5 \times 10^5$ cm^{-3} and a mass of $m \approx 2 \times 10^{-5}$ M$_\odot$.

The majority of clumps are of order 0.2 arcsec in diameter, or around 150 au. Assuming that the clumps are roughly spherical and have similar density, the mass of such a clump becomes m $\approx 5 \times 10^{-6}$ M$_\odot$.

At these densities (noting that $n_{H_2} = 0.5 n_H$) the globules can be in pressure equilibrium with the surrounding ionized gas. The density in the ionized gas is approximately n$_e = 1.3 \times 10^3$ cm^{-3} and the temperature is around 9000 K (Ueta & Otsuka 2021). Pressure equilibrium would be reached for a globule temperature and density T $\approx 50 \times 10^6/n_H$ K, or $T \sim 100$ K for a density $n_H \sim 5 \times 10^5$ cm^{-3}. The globules could therefore be essentially stable and avoid collapse or dissipation, until the surrounding gas recombines. Whether they are indeed in pressure equilibrium or are still collapsing depends on

Figure 5. MIRI images combining the direct mapping images and the simultaneous images of the Ring Nebula which extend the imaged field further to the north and west.
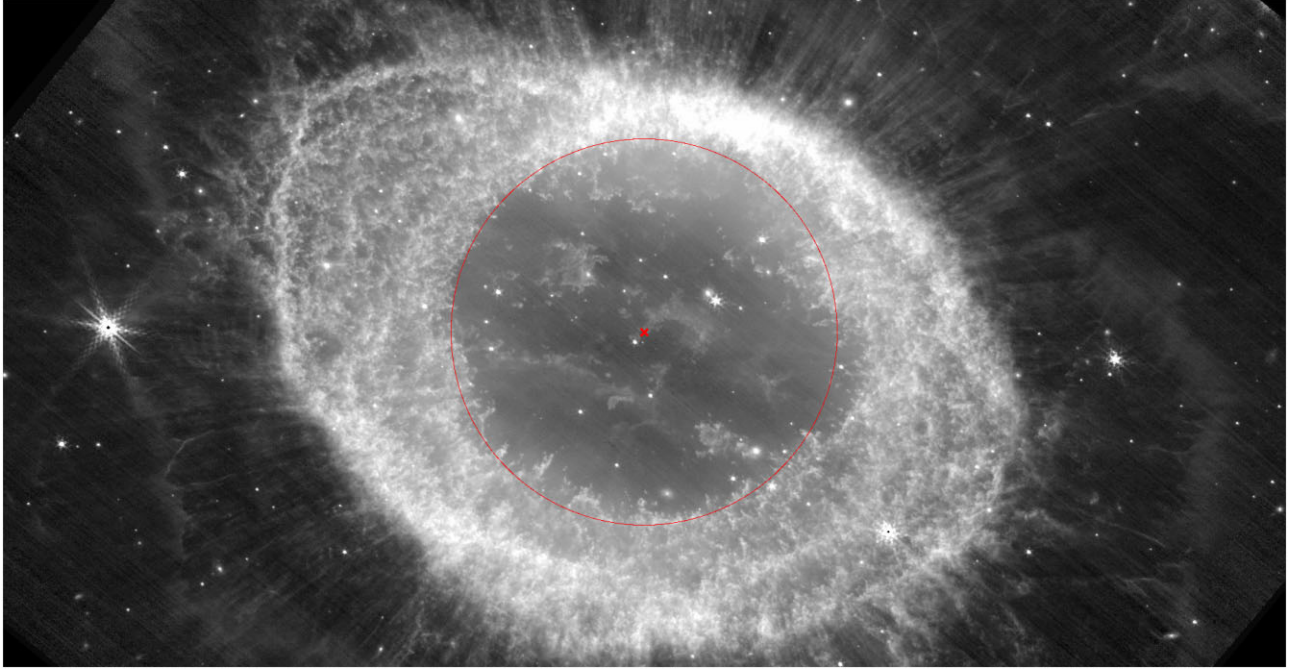
Figure 6. The boundary of the inner cavity of the Ring Nebula is close to circular, but its centre (marked by an X) is offset by 2 arcsec from the central star. The image is in the F335M filter. North is at the top, east is left.
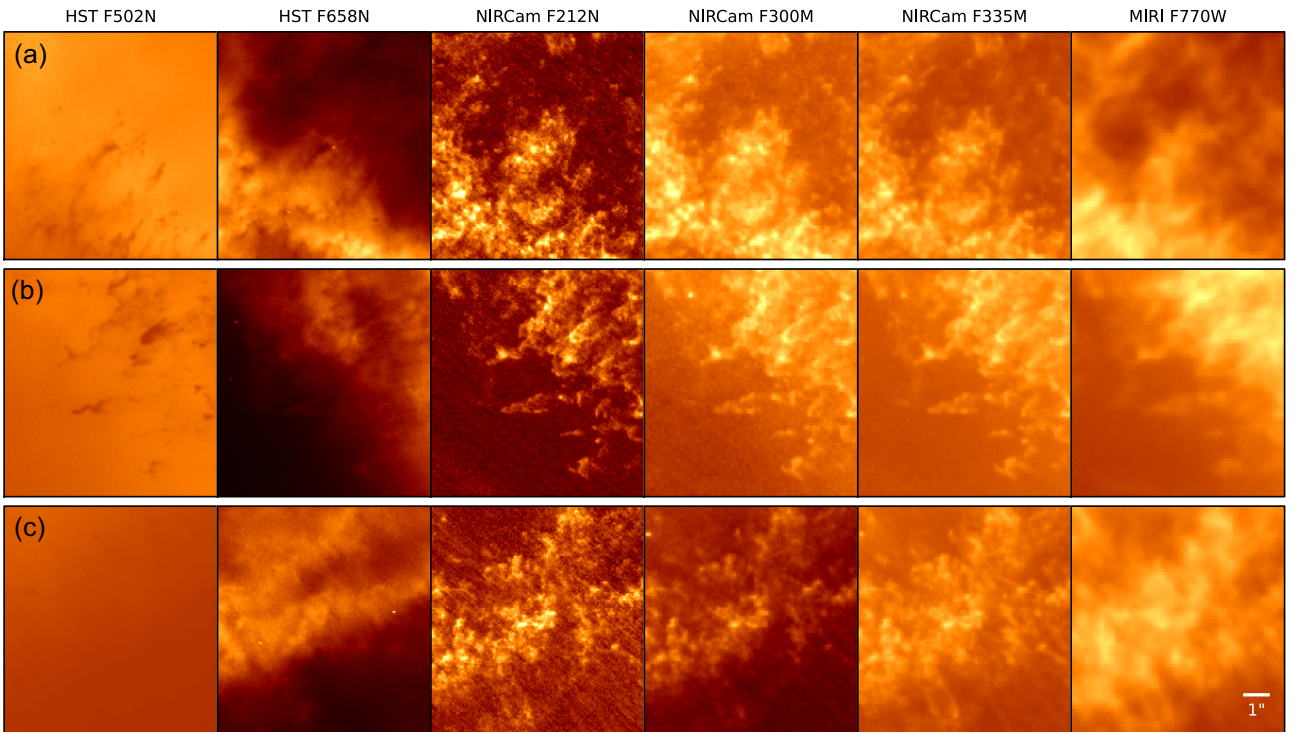
Figure 7. Zoomed-in images of globules in the Ring Nebula. The locations of the three zoomed-in regions are indicated in Appendix Fig. C3. Globules are detected in H_2 emission in the *JWST* NIRCam images and MIRI images, while some of them are seen in absorption against the diffuse ionized emission in the *HST* F502N and F658N images.
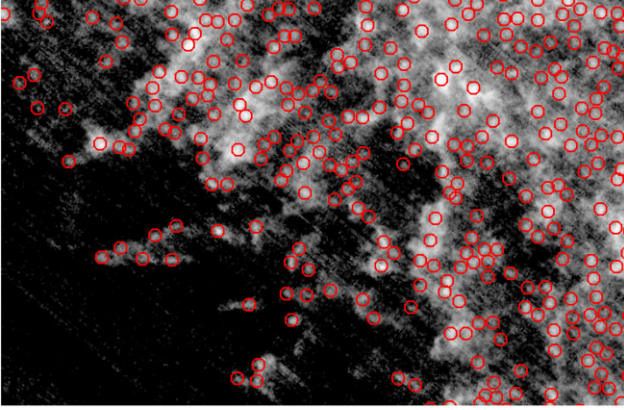
Figure 8. The positions of clumps, shown in red, identified by a peak-finding algorithm in a section of the main ring in the F212N image.

the unknown temperature, turbulence and details for the formation process.

Even the angular resolution of the *JWST* images does not allow the system of globules to be cleanly resolved. However, to estimate their total number, we applied a peak-finding algorithm from the PYTHON package PHOTUTILS (Bradley 2023) to the F212N image. A small section of the image is shown in Fig. 8, with the locations of the peaks found by the algorithm indicated. The peak-finding algorithm identifies about 17 500 peaks, which, given the density of clumps and resulting overlap, is likely to be an underestimate of the total number. A manual count was done in small regions, which, extrapolated to the full area, gives an estimated population of ∼25 000 globules.

Based on these numbers, the clumps have a combined mass of up to $0.1\,M_\odot$. In comparison, the CO emission also traces $\sim 0.1\,M_\odot$ (Bachiller et al. 1989). The molecular mass is similar to that found for NGC 3132 (De Marco et al. 2022).

The typical filling factor of dense clumps in PNe has been estimated as 7×10^{-5} (Zhang et al. 2004). In the Ring Nebula, this factor appears considerably higher: the clump filling factor for the shell is $\sim 2 \times 10^{-3}$. The density of the ionized gas in the shell in which the globules are embedded is around $1.3 \times 10^3\,\mathrm{cm}^{-3}$ (Ueta & Otsuka 2021). This gives an ionized mass in the shell of roughly $0.15\,M_\odot$. The clumps may therefore account for up to half the mass of the shell. Ueta & Otsuka (2021) argue for a similar ratio.

Sahai et al. (2012) used [C II] observations made with the Stratospheric Observatory for Infrared Astronomy (SOFIA) to show that $0.11\,M_\odot$, half the mass of the nebula, lies in a photon-dominated region (PDR) zone. Liu et al. (2001) found densities of $n_H \sim 10^5\,\mathrm{cm}^{-3}$ for these PDR regions. The PDR emission zone is likely associated with the clumps. The PDR zone is mixed in with the ionized gas, in a region where clumps and ionized gas coexist, rather than forming a separate outer shell. This zonal mixing is also seen in the ionized gas (e.g. Garnett & Dinerstein 2001).

The H_2 images reveal few cometary tails emanating from the globules. This is in contrast to the Helix Nebula where the majority of the globules (at least in the inner region) have well-developed tails seen in H_2 (Matsuura et al. 2009). Some short extensions of around 1 arcsec in length can be seen in absorption in the *HS T* F502N and F658N images (Fig. 7a,b) but these do not have clear counterparts in the *JWST* images. An exception is the largest globule in Fig. 7b, which shows a faint bow shape in the *HST* F658N image that becomes a longer 'U' shape in the *JWST* F300M and F335M

images. The extensions seen in the *HST* images tend not to be straight. They may trace an early stage of tail formation.

4.4 Radial spikes

The halo shows multiple narrow, radial features pointing away from the central star, which following De Marco et al. (2022) we call 'spikes' (Figs 9 and 10). [6] They are seen only outside the bright shell, and mainly in H_2. The spikes are mainly a feature of the inner halo (O'Dell et al. 2013a).

In a section of the F770W image covering $20°$ of azimuth, we count 15–20 spikes. From this, we estimate that there are about 300–400 spikes in total. The exact number is imprecise due to the low contrast, small separation, and partial overlap of many spikes. The typical width appears to be around 0.4 arcsec. The typical length of the visible spikes is around 20 arcsec, but they may in a few cases extend twice as far, to the outer edge of the nebula.

The spikes are expected to arise from illumination effects where stellar light escapes through holes in the shell (De Marco et al. 2022). They line up better with the central star than with the offset centre of emission, which indicates that the dominant cause lies in the current or recent radiation from the star. There are some cases of misalignment with the star, possibly where there is partial overlap between spikes.

The number of spikes is of order 2 per cent of the number of globules. This suggests that there is no direct relation between the globules and spikes. O'Dell et al. (2013a) argue that some of the spikes can be the shadows of large globules but this is not evident from the data here.

4.5 Arcs – concentric structures

A series of faint, broken concentric arcs is apparent outside the bright ring in the H_2 halo. In places, up to 10 arcs can be identified (Fig. 9). In some directions, the arcs appear to have been disrupted, possibly due to density variations in the nebula, but in general the curvature is regular (Fig. 10).

The concentric structures are most apparent in the F770W image, which contains emission lines of H_2, H I, and [Ar II]. They are also clearly visible in the F1000W and F1130W images and can be distinguished at longer wavelengths in the F1800W and F2100W filters, but at lower contrast due to the poorer spatial resolution. At shorter wavelengths with better spatial resolution, the much clumpier appearance of the nebula in the lines isolated by these filters makes the features harder to trace. The arcs are seen in most directions but are obscured by the shell along the major axis.

To highlight the radial and concentric structures, we reprojected the MIRI F770W image into polar coordinates relative to the central star. We then applied the edge-detection algorithm of Canny (1986) to the reprojected image. The result is shown in Fig. 10. Within the shell, the edges are primarily azimuthal, that is, horizontal in the azimuth–radius plot. Further out, the edges abruptly change to radial (i.e. vertical). This confirms that the spikes start suddenly at the outer radius of the shell. There is a region of overlap between the horizontal arc lines and the vertical spikes.

Using a portion of the F770W image in which the arcs are most clearly seen, we measure an average separation of about 1.5 arcsec. Assuming that the arcs are embedded in the outflow and are in the

---

[6]O'Dell et al. (2013a) uses the term 'rays'.
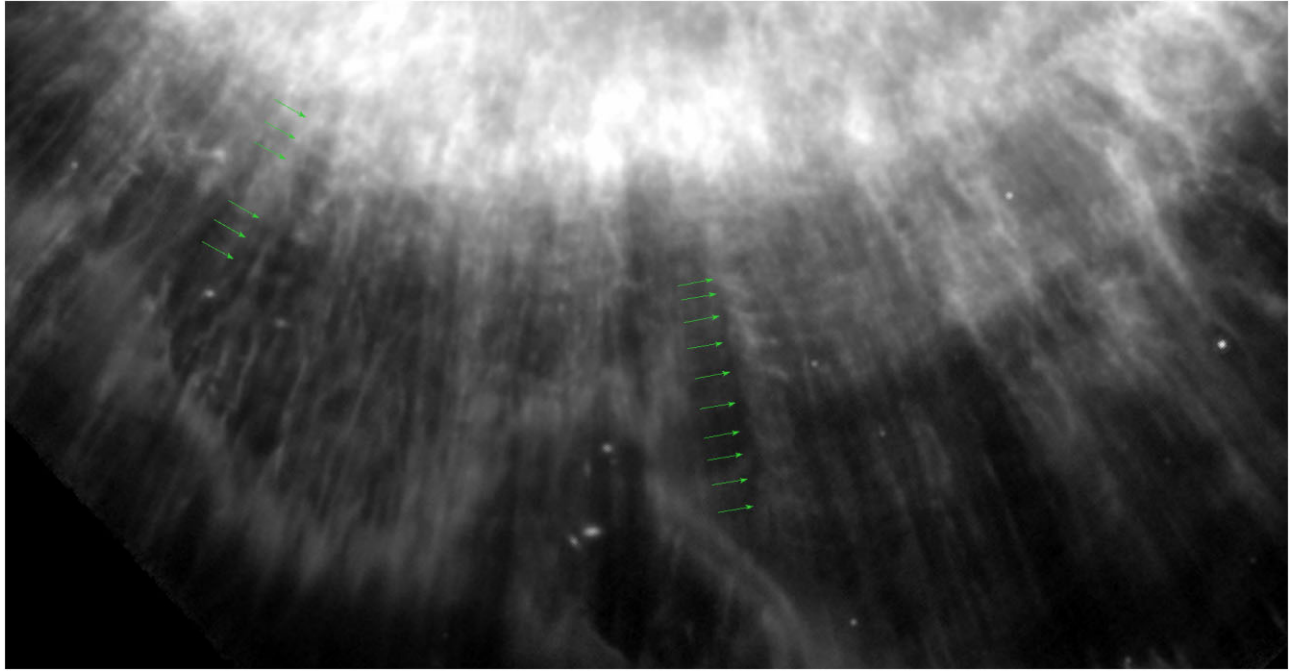
Figure 9. Regular concentric features in the outer regions of the F770W image of the Ring Nebula. Green arrows indicate the locations where these regularly spaced features are most easily seen.

plane of the sky, this separation and outflow velocity provide a time-scale. The outflow velocity of the Ring Nebula decreases outward from $\approx$40 km s^{-1} in the cavity to 20–25 km s^{-1} in the shell and 15 km s^{-1} in the halo (O'Dell et al. 2013a; Martin, Prunet & Drissen 2016; Sahai et al. 2012). We assume a value of 20 ± 5 km s^{-1} at the location of the arcs, just outside the shell. At a distance of 790 pc, this separation corresponds to a time interval of 280 ± 70 yr. This is much too short an interval to be related to periodic thermal pulses that may enhance mass-loss, which are expected to occur at intervals of 10^4–10^5 yr.

A common scenario invoked to explain arc systems like these is one in which a close binary companion modulates the outflow from the AGB star. The time interval of 280 yr then corresponds to the orbital period of the companion. If the combined mass of the original AGB star and its companion is $1.5 \pm 0.5 \, M_\odot$, the orbital separation would be about 50 ± 15 au.

JWST images of the Southern Ring Nebula (NGC 3132) have revealed very similar concentric structures, with a separation of about 2 arcsec at a distance of 750 pc. These have also been attributed to the effects of a binary companion, with an orbital period of 290–480 yr (De Marco et al. 2022). In the Southern Ring, the binary hypothesis is supported by the dust disc, which has an inner radius consistent with the inferred separation of the companion star, as indicated by the arcs.

Non-binary causes of the concentric arcs can be considered; these would need to fit the regular spacing, the time-scales and the azimuthal symmetry. Thermal pulses can be ruled out because they occur on much longer time-scales. Sahai et al. (1998) presented two classes of non-binary models which could create arc-like structures. For one of these, which invokes instabilities in the dust condensation and wind acceleration region, support comes from detailed 1D numerical modelling (Simis, Icke & Dominik 2001). However, it is unclear whether the instabilities produced in such models will show the azimuthal coherence necessary to produce extended arc structures.

As a final suggestion, many long-period Mira variables have period fluctuations of order 10 per cent, dubbed 'meandering Miras' (Zijlstra & Bedding 2002). These period changes have been suggested to lead to mass-loss variations and to swept-up shells as faster and slower winds interact, thus forming rings around PNe (Zijlstra & Bedding 2002). However, the period variations happen on faster time-scales, of order 50 yr, and they are not periodic (Merchan-Benitez, Uttenthaler & Jurado-Vargas 2023).

We thus consider the binary hypothesis to be the most likely explanation for the arcs in the Ring Nebula. More detailed hydrodynamical modelling would be necessary to determine whether any of the other possible mechanisms could fully reproduce the extent and regularity of the arcs.

5 DISCUSSION

5.1 PAHs

The PAH feature at 11.3 μm has been detected in *Spitzer* spectra of the Ring Nebula (Cox et al. 2016) based on programme 40536 (P.I. H. Dinerstein). *Spitzer*'s Infrared Spectrograph (IRS) covered a 99×18 arcsec area along the major axis of the elliptically shaped Ring Nebula, with a pixel scale of 1.8 arcsec. This spectral map showed that the PAH feature is emitted from the outer half of the shell, a more or less similar emitting region to the H$_2$ S(1) and S(2) lines at 17.04 and 12.28 μm.

The higher angular resolution *JWST* images allow the PAH-emitting regions to be studied in much more detail. The F335M filter encompasses the 3.3 μm PAH feature, while the F300M filter lacks this band but otherwise contains similar nebular emission (Table 1). The F1130W filter has the lowest contribution from
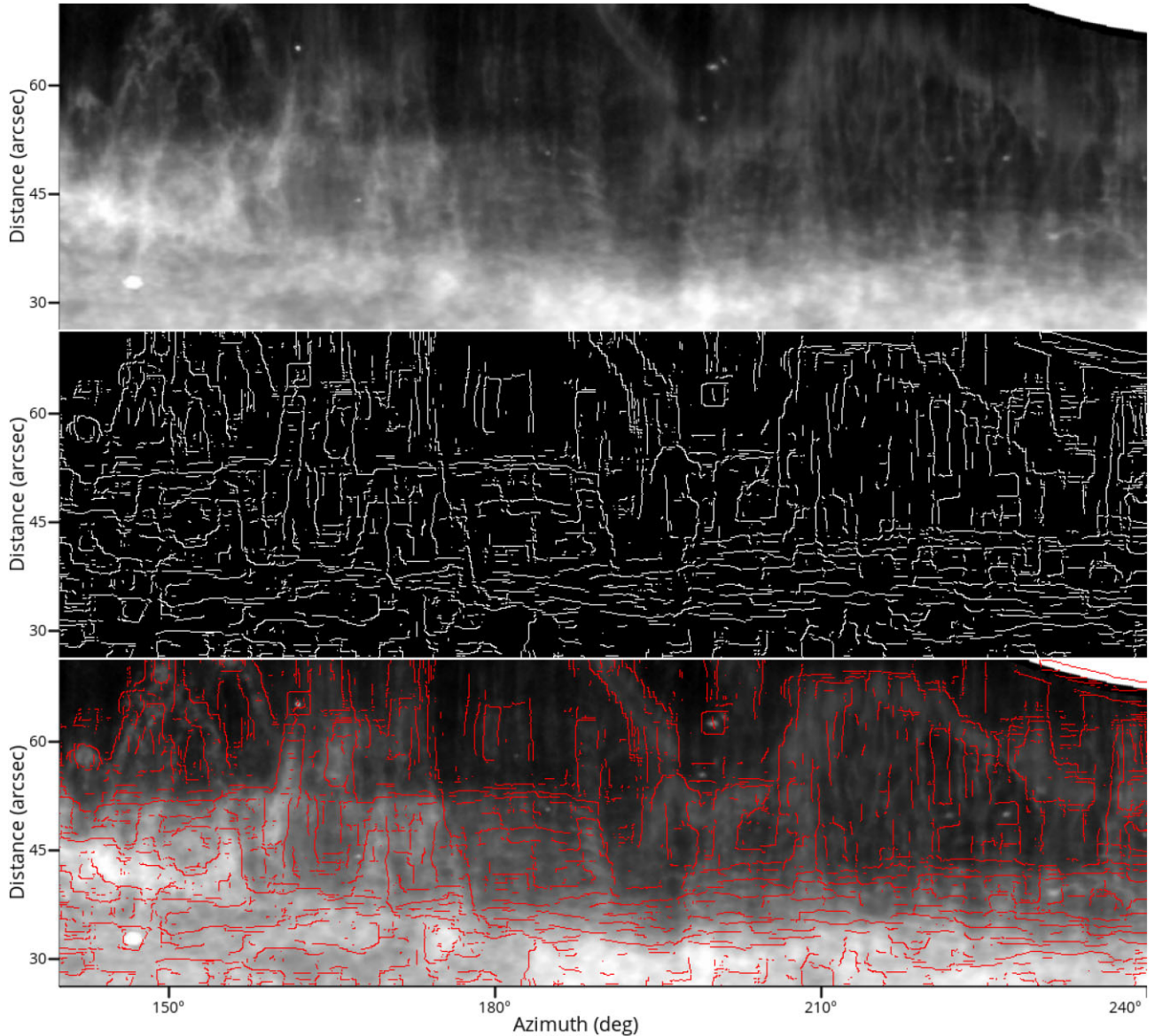
Figure 10. Application of an edge-detection algorithm to a section of the polar-projected image, highlighting the predominantly radial and concentric nature of the nebular structures. Top: reprojected F770W image. Centre: edges detected using the algorithm of Canny (1986). Bottom: edges overlaid on the reprojected image. The horizontal direction is azimuthal direction from north via east, and vertical direction is radial distance from the central star.

emission lines (Table 1), and best reflects the contributions of the continuum and PAH bands. Both the F335M/F300M ratio image and the F1130W/F1000W ratio image (Fig. 11) show indications of a narrow ring of excess emission located at the outer edge of the shell.

This narrow ring shows up only in the two filters containing PAH bands (Fig. 11) and is not seen in other filter combinations (Appendix Figs B1 and B2). From Table 1, the PAH contribution to F335M and F1000W is <14 per cent and <7 per cent, respectively, but this is estimated from MIRI IFU spectra which are not centred on the narrow ring; Appendix Fig. C3). We interpret these narrow ring excesses as possible PAH emission.

Fig. 12 presents the spectra of three different regions across the nebula, from the centre to the west, indicated as regions 1–3 in Fig. 11. The spectra were extracted from the *Spitzer* spectral map specified earlier. Region 1, the innermost region of the ring, lacks PAH emission at 11.3 μm but shows strong [S IV] emission in the

JWST F1000W filter. Further from the central star, the F1000W image is dominated by continuum emission, as found in the MRS North Region spectra (Table 1; van Hoof et al. in preparation). Regions 2 and 3 both show an excess of the F1130W over the F1000W flux, relative to a simply rising continuum, suggesting the presence of PAH emission. Also for these two fields, the F335M flux has a subtle excess over F300M. These two filter bands need cautious interpretations, as both contain several H_2 lines. Nevertheless, these excesses appear at the same locations, so we interpret them as being likely due to PAH emission.

Fig. 13 zooms in the north part of the Ring. The contours of the F335M/F300M ratio image are overlaid on the other three panels: the F1130W/F1000W ratio image, F162M, and F212N. The contours demonstrate that the peak of the F335M/F300M ratio, presumed PAH emission, is outside of the F212N H_2 emission. F162M is continuum-dominated (Table 1), and its continuum morphology resembles the
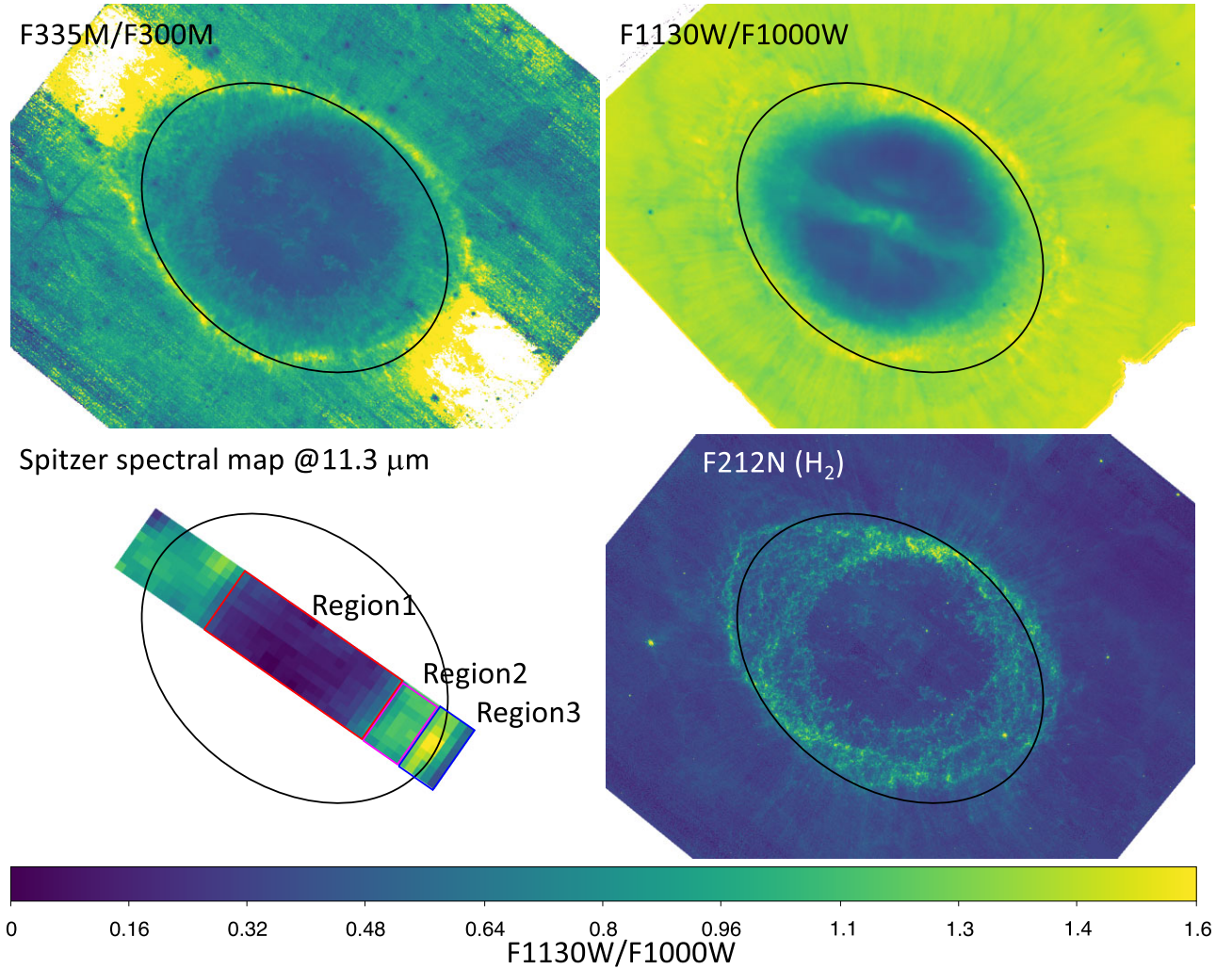
Figure 11. F335M/F300M ratio (top left), F1130W/F1000W ratio (top right) and *Spitzer* spectral map at 11.3 μm (10.95–11.65 μm, corresponding to *JWST* F1130W filter) (Cox et al. 2016) on the same scale (bottom left). The narrow ring at the edge of the shell, indicated by a black ellipse, is interpreted as the location of PAH emission. For comparison, the F212N H_2 image is shown at bottom right. The *Spitzer* spectra were extracted at three different regions and plotted at Fig. 12. North is at the top.

$H\alpha$ image (O'Dell et al. 2013a), suggesting that the continuum is due to free–free and bound–free from ionized gas. The zoomed-in image shows the stratified structure of ionized gas, H_2 and PAHs, separated in the radial direction. The [N II]/[O III] ratio (O'Dell et al. 2013a) also indicates a rapid fall-off of hard-UV radiation in this region.

The narrow colour-excess ring seen in Fig. 11 is centred on the current location of the central star, rather than the offset centre found for other emission features, and follows the outer contour of the H_2 distribution. As noted, the nebula consists of lower density ionized gas, in which the dense globules are embedded. The PAHs show a clumpy distribution, but PAH emission associated with the H_2 globules is much fainter: the surface brightness of PAH emission at the position of the H_2 globules is about 1/3 of the peak. The gas density of the nebula is not uniform, and just inside the ionization front, the nebular gas has a higher density, and is optically thick to the harder, H-ionizing UV photons at this front. The presence of PAH emission beyond the ionization front shows that PAHs are excited by UV or optical radiation that has a lower energy than the H-ionizing energy. Whether the clumpy distribution of the PAH emis-

sion traces density variations and UV photon flux variations is not clear.

Whilst the H_2 emission is widespread in the nebula, PAH emission is much more localized. However, we cannot conclude that weaker PAH emission is not present elsewhere in the nebula. Neither can we conclude whether the PAHs are created by the chemistry in the narrow ring or have survived from the molecular AGB wind.

5.2 Multiplicity

A distant companion to the central star was identified by González-Santamaría et al. (2021). This star, *Gaia* DR3 2090486687506009472, lies 18.5 arcsec from the central star, corresponding to a projected distance of 0.07 pc. It shares both the proper motion and parallax of the central star, and is the only *Gaia* star within 5 arcmin to do so. González-Santamaría et al. (2021) proposed that this companion is a white dwarf, based on the *Gaia* DR3 photometry. However, the B_P and R_P photometry is discrepant from the G-band photometry by 2.74 mag, and appears to be significantly affected by nebular emission lines. Similar problems appear to affect other
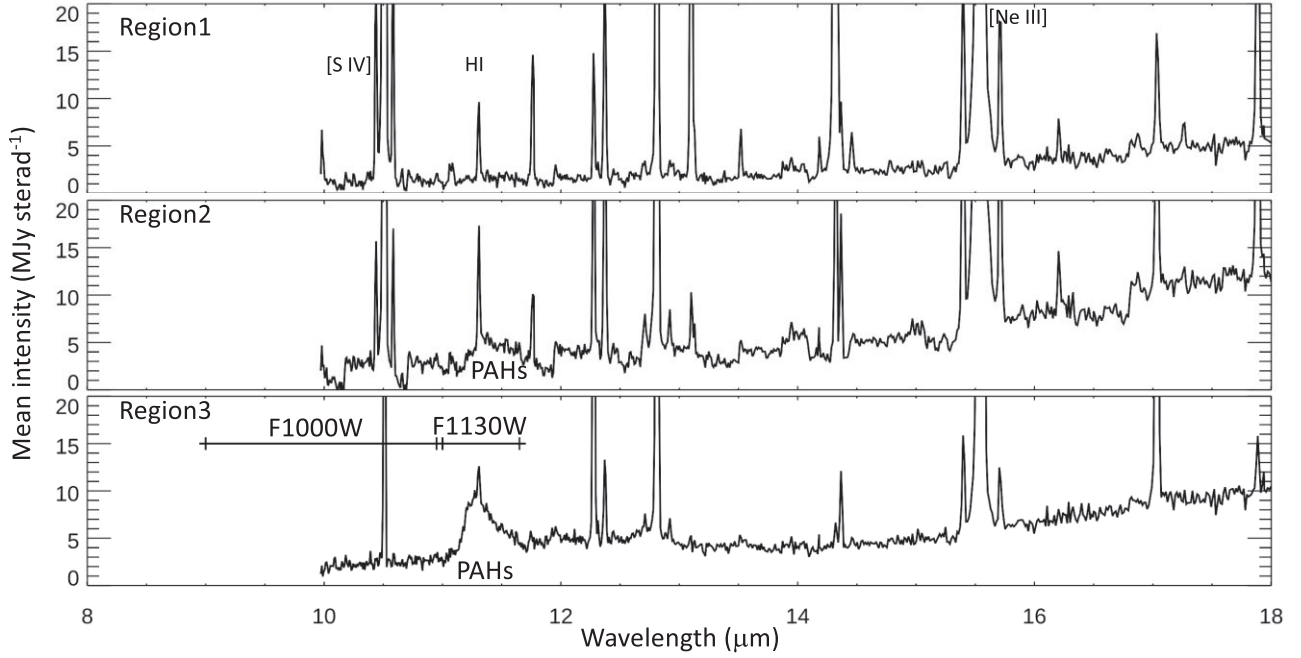
Figure 12. The extracted *Spitzer* spectra of the Ring Nebula (Cox et al. 2016), from the top towards the inner ring from region 1 to 3. (Fig. 11). Region 3 has an excess of PAHs at 11.3 μm in Fig. 11, and *Spit zer* spectra confirm the presence of 11.3 μm PAHs, while region 1, the innermost region of the ring, lacks observed PAHs.
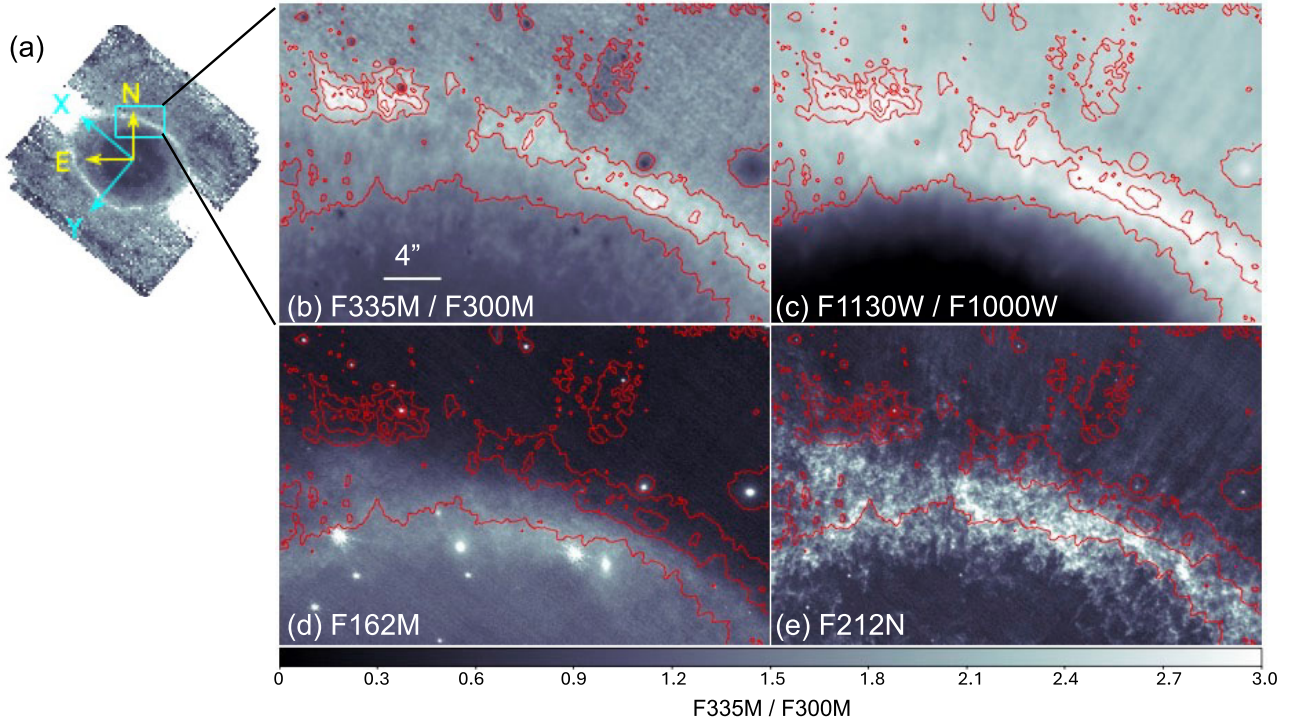
**Figure 13.** Images of a small region in the north part of the Ring Nebula, indicated in panel (a); (b) F335M/F300M, (c) F1130W/F1000W, (d) F162M, and (e) F212N. The contour lines at the levels of 1.5, 2.12, 2.6 of the F335M/F300M ratio maps are plotted in panels (b–e), indicating the relative locations of the emitting regions of the F335M/F300M ratio (PAHs), F162M (continuum, free–free and bound-free), and F212N (H_2).

optical and near-IR photometry of the star (Chambers et al. 2016; Skrutskie et al. 2006), which are discrepant from both the photometry published in the Hubble Source Catalogue (Whitmore et al. 2016) and from the *Gaia* photometry.

The available photometric data for this star are presented in Fig. 14. This figure includes photometry from our NIRCam and MIRI observations, extracted with an aperture of radius 1 arcsec. The 'background' for these *JWST* data points was estimated in an annulus
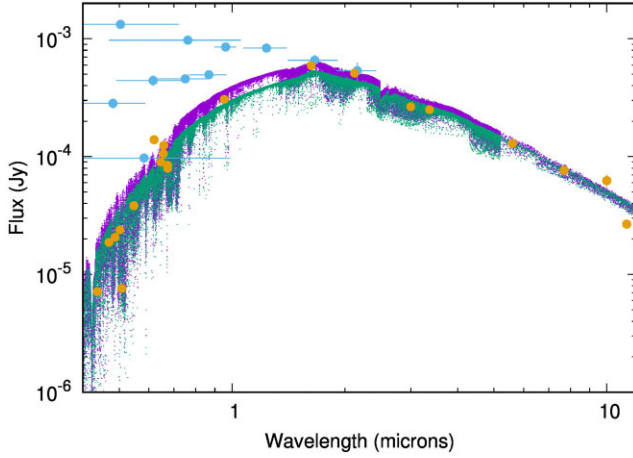
Figure 14. SED of a companion star candidate, *Gaia* DR3 2090486687506009472. Orange points show archival *Hubble Space Telescope* photometry and our new *JWST* photometry. Blue points show other literature data from *Gaia*, the Two Micron All-Sky Survey (2MASS) and the Panoramic Survey Telescope and Rapid Response System (Pan-STARRS) as indicated in the text. Many of these are strongly affected by the bright nebular background. Overlain are BT-SETTL model atmospheres (Allard 2014) for 3400 K and 3600 K stars with log (g) = 4.5 dex, [Fe/H] = –0.5 dex, [α/Fe] = +0.2 dex, and the appropriate reddening.

Table 2. PYSSED parameters of the companion star, for two values of the metallicity.

[Fe/H]	0.0	−0.4
T_{eff}	3281–3406 K	3382–3635 K
L	0.0136–0.0199 $L_\odot$	0.0328–0.0433 $L_\odot$
R	0.362–0.406 $R_\odot$	0.525–0.604 $R_\odot$

of inner/outer radii of 1.1/1.5 arcsec, with the aperture correction estimated using WebbPSF.

To establish the properties of the companion star, we use the Python Stellar Spectral Energy Distribution toolset (PySSED),[7] an SED-fitting code based on the software presented in McDonald et al. (2009), McDonald, Zijlstra & Boyer (2012), McDonald, Zijlstra & Watson (2017). We assume a distance to the star of 790 pc, and that the star has a composition of between [Fe/H] = −0.4 and +0.0 dex and a corresponding [α/Fe] = +0.1 to + 0.0 dex, based on its height of 190 pc from the Galactic plane. The Ring Nebula has a metallicity which is approximately solar (Liu et al. 2004; Guerrero, Manchado & Chu 1997).

The most significant unknown is the extinction by dust in the nebula at this location, which also depends on whether the star is in front or behind the main shell. We assume a plausible range of $c_{\mathrm{H}\beta}$ = 0.1 to 0.4, giving $E(B - V) = c_{\mathrm{H}\beta}/1.46$ = 0.068 to 0.274 mag. Assuming that the extinction is the dominant source of uncertainty, we fit the parameters listed in Table 2.

These correspond to a main sequence star of approximate spectral type M2–M4 with a mass of 0.3–0.5 $M_\odot$ (Cifuentes et al. 2020).

At the projected distance of the companion from the central star, the orbital period would be of order 10^6 yr and the orbital velocity 250 m s^{-1}. If the star was bound before the AGB mass-loss, it is

---

[7] PySSED is the code underlying the S-Phot software data application. It is currently under development and will be hosted at https://explore-platform.eu/sdas

likely unbound now. It is plausible that it was originally in a more compact orbit. However, the proper motion shows that it cannot have moved away by more than 3 arcsec during the lifetime of the PN.

Although the companion star lies roughly along the direction of the minor axis, it is not exactly aligned: the offset is about 25°.

The concentric arcs indicate the additional presence of a closer companion, with an estimated period of 280 yr, corresponding to a semimajor axis of 50 au for an assumed combined mass of 1.5 $M_\odot$. This is similar to NGC 3132 where there is also evidence for at least a triple stellar system.

The puzzling 2 arcsec offset between the centre of certain nebular structures and the central star could be related to the multiplicity. A speculative model for this involves an elliptical orbit for the close pair. As most of the time in an eccentric orbit is spent near largest separation (apoastron), the nebula is ejected with a typical central velocity corresponding to this part of the orbit. The offset acquired over a dynamical time of 4000 yr corresponds to a velocity of 2 km s^{-1}. For the system above and assuming an ellipticity of 0.5, a velocity difference of the primary component between systemic and aphelion of 2 km s^{-1} requires an equal-mass binary. It should be possible to detect a main-sequence star with such a mass, but a white dwarf companion would be difficult to see.

The companion star has remained bound to the central star over its lifetime. Assuming that it formed at this distance, this suggests that no other star has come closer to it than half the current separation of 0.07 pc. For an assumed number density of stellar systems of 0.1 pc^{-3}, the mean free path is 2600 pc. Assuming a random velocity of 10 km s^{-1}, this gives a time between encounters of 1 Gyr. This is an indicative calculation only, but it favours a higher-mass progenitor for the central star of $\gtrsim 2\,M_\odot$ because of the evolutionary time-scales. A more massive system is also more robust against perturbations. Alternatively, the companion may have formed in a tighter orbit and escaped due to the AGB mass-loss of the primary. This requires a mass-loss of 50 per cent or more of the original combined mass, which also indicates a primary progenitor mass of 1.5 $M_\odot$ or more.

5.3 Comparison to similar PNe

The two well studied PNe which are most similar to the Ring Nebula are the so-called Southern Ring Nebula and the Helix Nebula.

NGC 3132 (the Southern Ring Nebula) lies at a similar distance, at 750 pc. It was imaged with *JWST* as part of its Early Release Observations (ERO) programme (Pontoppidan et al. 2022). A detailed analysis of these images was carried out by De Marco et al. (2022). NGC 3132 was imaged in fewer filters than NGC 6720 (the Ring Nebula), but the images show very similar structures to those we find here, including the numerous globules visible in H$_2$, the radial spikes in the halo, the system of concentric arcs and the structure inside the cavity.

The Helix Nebula is closer to us, at 200 pc. It too has a system of globules, but the globules in the inner part of its shell have well defined tails (O'Dell, McCullough & Meixner 2004; Matsuura et al. 2009), which are rarely seen in NGC 6720 and NGC 3132. Spikes in the halo are detected in the *Spitzer* 5.8 μm image of the Helix (Hora et al. 2006).

It is interesting to note that the numbers of globules in each of these three nebulae are similar, of order 20 000 (Meixner et al. 2005; De Marco et al. 2022). Applying the same peak-finding algorithm that we used to count the clumps in the Ring Nebula (subsection 4.3) to the Southern Ring Nebula we find 15 000 clumps. However, there are notable differences in the size and shape of globules in the Ring Nebula compared to the other two objects. The Helix globules

typically have a diameter of 2 arcsec in H_2 images (Matsuura et al. 2009) at a distance of 200 pc, and one of the largest globules in the Southern Ring Nebula is 0.5 arcsec in diameter at a distance of 750 pc (De Marco et al. 2022). These angular diameters correspond to ~400 au. In contrast, the globules in the Ring Nebula tend to be smaller. One of the largest globules in the Ring Nebula is indicated in Fig. 3. The diameter of the head is approximately 0.4 arcsec across in the F212N H_2 image, corresponding to 300 au. The typical diameter of the globules is 0.2 arcsec, or 150 au. Most of the Ring Nebula globules also lack significant tails.

Another similar PN of relevance is NGC 2346, which has been imaged in H_2 from the ground (Manchado et al. 2015). It has a more flaring bipolar structure with a thinner torus than the Ring Nebula, but the torus shows similar H_2 clumps. The clumps range in size from 0.16 to 0.34 arcsec which, at a *Gaia* DR3 distance of 1400 pc, corresponds to between 200 and 500 au. This is larger than for the Ring Nebula but similar to those in the Southern Ring and the Helix Nebula.

5.4 Fragmentation, H_2, and PAHs

The formation mechanism of the globules is still under debate. Globules may form before the ejection of the PN, and survive in the circumstellar medium (Zanstra 1955), or alternatively, they may have formed during the PN phase (Capriotti 1973; García-Segura et al. 2006). The central stars of the four PNe described in subsection 5.3 are all on the cooling track in the HR diagram. This supports a model in which the globules form after the rapid fading of the central star on the cooling track of the white dwarf phase, as a result of recombination of the dense gas of the shell (O'Dell, Sabbadin & Henney 2007; van Hoof et al. 2010). Further support for a picture where clump formation occurs predominantly at late times, rather than before the ejected envelope has been ionized, was found by Huggins & Mauron (2002), who demonstrated the absence of small scale structures in objects in the early stages of transition from proto-PNe to full-fledged PNe.

During recombination, the recombination rate (t_{rec}) is faster in denser regions ($t_{rec} = 10^5$ yr/n_e for hydrogen). If density fluctuations are present, the higher density regions will recombine first, lose electron pressure, and collapse under the pressure of the surrounding ionized gas, which will be ~200 times higher than in the recombined regions. Molecules and dust can form, shielded and shielding against the UV radiation. The effect of this shielding can be seen via extinction by the neutral globules against the ionized gas background emission and shadowing in the tails. This process, where the globules form by recombination and compression can explain the location and the properties of the globules.

The tails in the globules of the Helix nebula are best explained by shadowing (Cantó et al. 1998; Andriantsaralaza, Zijlstra & Avison 2020) within the photo-ionized region, triggering recombination and allowing CO to form along the tail (Andriantsaralaza, Zijlstra & Avison 2020). Involvement of stellar wind ablation in tail formation (Dyson et al. 2006; Matsuura et al. 2007) cannot be excluded, but stars on the white dwarf cooling track do not have strong stellar winds.

The lack of tails in the Ring nebula may point to it being in an earlier stage of evolution. The shell of the Helix Nebula is larger than those of the other nebulae, at a radius of 0.33 pc (O'Dell, McCullough & Meixner 2004) versus 0.1 pc for NGC 6720 and 0.07 pc for NGC 3132. The Helix Nebula has a larger dynamical age of ~ 7400 yr (González-Santamaría et al. 2021) and has likely been on the cooling track for longer.
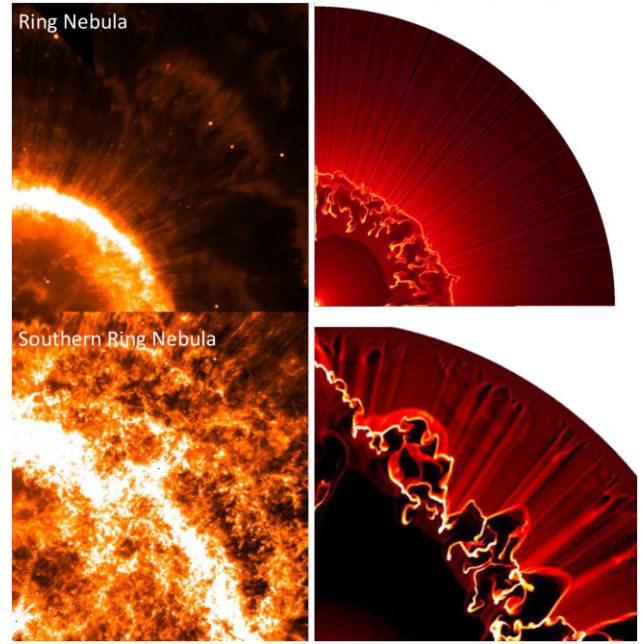
Figure 15. (Right) Density snapshot of a hydrodynamic simulation for the Ring Nebula (right top) and the Southern Ring Nebula (right bottom). The hydrodynamic model for the Southern Ring Nebula is taken from De Marco et al. (2022). (Left) *JWST* images of the Ring Nebula (top left; F770W) and the Southern Ring Nebula (bottom left; F212N), highlighting the spikes and clumps. The Southern Ring Nebula has evolved faster, and has more fully developed spikes and clumps.

On the cooling track, the star initially fades rapidly, leading to recombination. But the fading slows down dramatically after that (Miller Bertolami 2016). During this phase, the nebula keeps expanding and the density drops. Once the star stops fading, the ionization front should move outward through the nebula again, due to the expansion of the nebula and hence lower density and longer recombination time-scales. The ionization front can now pass the previously formed globules. Once that happens, the globules may develop tails in the shadowed region in the re-ionized gas. This could explain why the inner globules in the older Helix Nebula have tails, while those in the younger nebulae do not.

The difference in distribution between H_2 emission and PAH emission is notable. H_2 is widespread in the system of globules. If the globules formed by recombination, then the H_2 here formed in situ afterwards. PAH emission is bright at the outer edge of the H_2 globule-dominated zone. PAH formation in an oxygen-rich environment may require moderate UV radiation, acting through UV destruction of CO (Black & Dalgarno 1977; Guzman-Ramirez et al. 2011; Berné et al. 2023).

5.5 Hydrodynamical model

Fig. 15 shows density snapshots from hydrodynamical models (García-Segura et al. 2006; García-Segura, Ricker & Taam 2018) for the Ring Nebula and the Southern Ring Nebula. The models are extracted for an age of 4000 yr after envelope ejection, a time equal to the dynamical age of the Ring Nebula (O'Dell et al. 2013a). The 2-d simulation has a resolution of 1000×1000 zones in spherical polar coordinates (R, Φ) on the orbital or equatorial plane. The model assumes ejection via a common envelope evolution event which provides an equatorial density enhancement. There is currently no

evidence that the Ring Nebula underwent a common envelope event, since the posited binary companions are too distant to lead to a common envelope phase. However, the common envelope leads to formation of a high-density torus which is the structure of the shell of the Ring Nebula. The model follows the expansion of the ejected shell, and includes central star evolution (Vassiliadis & Wood 1994) and ionization of the nebula.

The model (Fig. 15) shows the formation of higher density regions in the form of clumps in a way similar to described earlier. They are formed due to the thin-shell instability in the swept-up shell. The thin-shell instability acts in wind-blown bubbles (Vishniac 1983) and is very effective at producing clumps (García-Segura & Mac Low 1995). It may involve photoionization. The number of clumps depends on the thickness of the swept-up shell, which is related to the temperature and pressure of the shell, and also depends on the expansion velocity.

Another instability can occur in thicker shells sandwiched between an ionization front and a shock front, which can fragment through a so-called I-S (ionization-shock) instability (Garcia-Segura & Franco 1996). This does not involve a wind. In the I-S instability the clumps form at the ionization front. In the model, the first mechanism acts, but both mechanisms can lead to clumping.

The clumps come into pressure equilibrium with the surrounding medium. This may provide a natural explanation for the clumps being larger in the Helix Nebula: it has expanded further with lower density in the ionized region, allowing the clumps to expand.

The I-S instability can form tails directly behind the clumps, caused by direct shadowing. The thin-shell mechanism does not form tails connected to the clumps, because of the hot-shocked gas and internal gas motions in the bubble. However, once the wind stops, tails can form progressively while the hot-shocked gas disappears, in the same way as for the I-S instability.

Fig. 15 compares the Ring Nebula with the Southern Ring nebula, with models for each (De Marco et al. 2022). The model for the Southern Ring corresponds to a slightly later phase in the evolution. Thus suggests an evolutionary order, Ring Nebula → Southern Ring → Helix Nebula.

The total numbers of globules in these three PNe are similar, of order 20 000. This suggests that the densities and expansion velocities of the nebulae were similar, as these two parameters are key to triggering the instabilities that initiated the formation of the globules.

5.6 Spikes

Narrow spikes are found in the halo of the Ring Nebula, the Southern Ring, and the Helix. Although rarely reported (e.g. NGC 6543; Guerrero et al. 2020), they may be a common phenomenon in PNe. They are seen in H_2 emission in the Ring Nebula, the Southern Ring (De Marco et al. 2022) and the Helix Nebula (Hora et al. 2006) but in optical emission in NGC 6543 (Guerrero et al. 2020). The latter paper presents a hydrodynamical model where the spikes appear to form behind holes in the dense shell.

The fact that the spikes are well aligned with the star shows the importance of illumination. There does not appear to be a direct relation between the spikes and the clumps; the spikes number only around 2 per cent of the number of clumps, and the clumps in the Ring Nebula do not have tails.

The spikes in the Ring Nebula are seen in H_2. They are likely excited by radiation passing through the shell. While the clumpy gas in the shell is optically thick for <912 Å radiation which can photoionize hydrogen, it can still be optically thin at >912 Å. Thus, longer wavelength UV radiation can escape through the swept-up

shell, exciting H_2 molecules via fluorescence in the remnant AGB wind.

The H_2 molecules in the halo are unlikely to result from recombination of the ionized gas, since recombination times in the halo are much longer than those in the main shell. The spikes therefore likely formed already during the high-luminosity PN phase on the horizontal track, and were shadowed during this phase which allowed the original molecules to survive while the surrounding halo became ionized.

The hydrodynamical model described above also produces spikes. They form in the halo where there is no hot shocked gas, again by shadowing. The lack of hot gas explains why spikes formed but tails did not. There are open issues: the model predicts a similar number of spikes and clumps, and because of the high density it has fast recombination.

Comparison of this work with that for the Southern Ring nebula (De Marco et al. 2022) shows that the spikes are less developed in the Ring Nebula. The mass of the progenitor star may play a role, as the central star of the Ring Nebula was likely of lower initial mass (~ 1.5–$2\,M_\odot$) than that of the Southern Ring ($2.86 \pm 0.06\,M_\odot$).

5.7 Halo

The *JWST* images show the presence of H_2 in the halo, for example in the F335M filter. The images show a combination of azimuthal structures further out and flocculent structure in the inner halo. The latter is mainly seen closer to the major axis, outside the shell.

Bryce, Balick & Meaburn (1994) proposed a biconical structure, with two lobes extending into the halo (their Fig. 11). This model was refined by Sahai et al. (2012) and O'Dell et al. (2013a). The bicone has a wide opening angle, and is confined by the torus which forms the shell. The polar axis is close to the line of sight, making the bicone not obvious in the images. However, the projected bicone is seen in longslit spectra, separated by its higher flow velocity.

We created a morphological model consisting of a barrel-like torus, and a wide bipolar flow angled $30°$ from the line of sight, towards the minor axis of the shell. The lobes start at the shell and move out into the inner halo. The lobe is assumed to be slightly flaring, with radius $r \propto z^{1.5}$. The H_2 is assumed to be located on the wall of the cone, swept out from the shell. This model is speculative.

Fig. 16 shows the F770W *JWST* image, with the contours of the wall of the cone superposed. In this model, the two cones are slightly separated in projection. Where the contours run close together, there is a longer line of sight along the cone and more H_2 emission may be expected. The contours roughly agree with the location of the H_2. Interestingly, it can also explain the two stripes seen in projection against the cavity which become the edge of the bicone. Finally, the arcs and stripes are both seen where the wall of the cones is seen under the most favourable angle, around the polar axis.

The model is overplotted on the F1800W/F1000W ratio image in the bottom panel of Fig. 16. F1800W is dominated by [S III] and F1000W by [S IV]. The latter is seen in the openings of the cones which provide a clear line of sight into the cavity. The lower excitation [S III] comes from the shell. The region between the stripes also shows this emission from the shell, projected on the cavity, and therefore has a very different appearance in the ratio image.

A similar structure is visible in the images of the Southern Ring (De Marco et al. 2022). However, there are notable differences between the two. Although the structure is along the major axis of the optical nebula in both cases, this corresponds to the equatorial axis in the Ring Nebula, but the polar axis in the Southern Ring. The region between the two lines is devoid of high-excitation emission in the
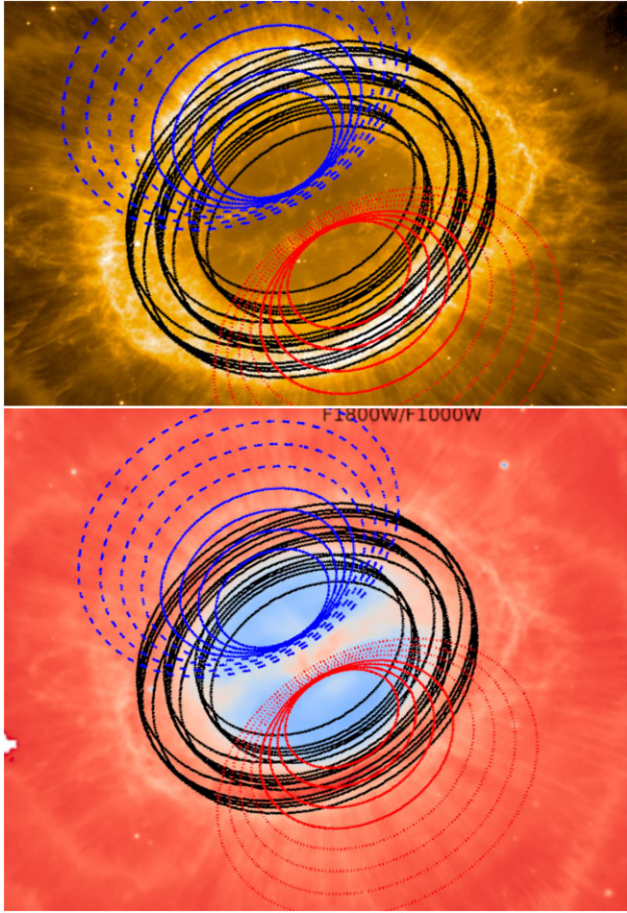
Figure 16. Top: The F770W images with the contours of the bicone superposed. Black lines show the torus, blue and red the cones. The dashed lines show the cone in the halo. Bottom: the same model superposed on the F1800W (red)/F1000W (blue) ratio image.

Ring Nebula, but is occupied by high-excitation gas in the Southern Ring. It appears that although the structures are superficially similar, they are not related. If both are related to polar flows, then this flow has a very wide opening angle for the Ring Nebula, but a very narrow one (chimney-like) in the Southern Ring.

6 CONCLUSION

JWST images have revealed a wealth of structural detail in NGC 6720. The nebula has a highly ionized inner cavity, a shell in which some 20 000 dense clumps contain up to half the total mass, a thin ring of possible PAH emission, and a halo that contains around 10 concentric arcs and 400 spikes. The centre of the nebula is offset by 2 arcsec from the central star. Much of this detail is shown by the H_2 emission.

The globules/clumps have densities of $n_H \sim 10^5$–10^6 cm^{-3} and account for ~ 0.1 M$_\odot$, up to half the mass of the PN. They are modelled as arising from thin-shell or I-S instabilities. The PNe in which clumps are seen have central stars that are already on the cooling track, suggesting that the clumps form during the rapid fading of the star. The globules in the Ring Nebula have little or no tails, unlike those in the Helix Nebula. The globules in the Helix are also larger. These differences could be due to the Helix Nebula being more evolved and the Ring Nebula being in an earlier phase of evolution.

The radial spikes in the halo are seen in H_2. They are regions partially shadowed by the shell, predicted by the hydrodynamical model.

The central exciting star is inferred to be a member of a triple system. This consists of: the central star itself, with a progenitor mass of ~ 1.5–2 M$_\odot$; a binary companion at some 50 au, responsible for the evenly spaced concentric arc structures in the nebula; and a distant, common proper motion companion at 0.07 pc which is a low-mass M2–M4 main-sequence star.

A schematic model is presented which consists of the central torus and two polar cones, in which the H_2 is swept up on the walls of the cones. The model can explain the location of the H_2 emission in the halo and the stripes seen on projection against the cavity.

Many features we see in the *JWST* images of the Ring Nebula, including the spikes, are shared by several other well studied PNe of similar morphology. The time when PNe could be modelled as uniform density spheres is long gone. They contain a wide variety of structures and phases, with very different conditions and size scales, ranging from highly ionized hot gas to dense molecular clumps.

DATA AVAILABILITY

JWST data are available from the Barbara A. Mikulski Archive for Space Telescopes (MAST; https://mast.stsci.edu). The raw data analysed in this paper are available at https://dx.doi.org/10.17909/bv01-qg73. Our reduced data products are available at MAST as a High Level Science Product via https://dx.doi.org/10.17909/c8k8-hz68.

REFERENCES

Allard F., 2014, in Booth M., Matthews B. C., Graham J. R., eds, IAU Symposium Vol. 299, Exploring the Formation and Evolution of Planetary Systems.Cambridge Univ. Press Cambridge, p. 271

Andriantsaralaza M., Zijlstra A., Avison A., 2020, MNRAS, 491, 758

Aniano G., Draine B. T., Gordon K. D., Sandstrom K., 2011, PASP, 123, 1218

Bachiller R., Bujarrabal V., Martin-Pintado J., Gomez-Gonzalez J., 1989, A&A, 218, 252

Balick B., Gonzalez G., Frank A., Jacoby G., 1992, ApJ, 392, L582

Berné O., et al., 2023, Nature, 621, 56

Black J. H., Dalgarno A., 1977, ApJS, 34, 405

Bohlin R. C., Gordon K. D., Tremblay P. E., 2014, PASP, 126, 711

Bouchet P., et al., 2015, PASP, 127, 612

Bradley L., 2023, astropy/photutils: 1.8.0

Bryce M., Balick B., Meaburn J., 1994, MNRAS, 266, 721

Bushouse H., et al., 2022, JWST Calibration Pipeline. available from https://doi.org/10.5281/zenodo.7229890

Canny J., 1986, IEEE Transactions on Pattern Analysis and Machine Intelligence PAMI-8, no. 6, 679

Cantó J., Raga A., Steffen W., Shapiro P. R., 1998, ApJ, 502, L695

Capriotti E. R., 1973, ApJ, 179, L495

Cardelli J. A., Clayton G. C., Mathis J. S., 1989, ApJ, 345, L245

Chambers K. C., et al., 2016, preprint (arXiv:1612.05560)

Cifuentes C., et al., 2020, A&A, 642, 115

Cox N. L. J., Pilleri P., Berné O., Cernicharo J., Joblin C., 2016, MNRAS, 456, 89

De Marco O., et al., 2022, Nature Astronomy, 6, 1421

Dyson J. E., Pittard J. M., Meaburn J., Falle S. A. E. G., 2006, A&A, 457, 561

Garcia-Segura G., Franco J., 1996, ApJ, 469, L171

García-Segura G., Mac Low M.-M., 1995, ApJ, 455, L160

García-Segura G., López J. A., Steffen W., Meaburn J., Manchado A., 2006, ApJ, 646, L61

García-Segura G., Ricker P. M., Taam R. E., 2018, ApJ, 860, L19

Gardner J. P., et al., 2023, PASP, 135, 068001

Garnett D. R., Dinerstein H. L., 2001, ApJ, 558, L145

González-Santamaría I., Manteiga M., Manchado A., Ulla A., Dafonte C., López Varela P., 2021, A&A, 656, 51

Gordon K. D., Engelbracht C. W., Rieke G. H., Misselt K. A., Smith J. D. T., Kennicutt Robert C. J., 2008, ApJ, 682, L336

Greenhouse M. A., Hayward T. L., Thronson Harley A. J., 1988, ApJ, 325, L604

Guerrero M. A., Manchado A., Chu Y. H., 1997, ApJ, 487, L328

Guerrero M. A., Ramos-Larios G., Toalá J. A., Balick B., Sabin L., 2020, MNRAS, 495, 2234

Guzman-Ramirez L., Zijlstra A. A., Níchuimín R., Gesicki K., Lagadec E., Millar T. J., Woods P. M., 2011, MNRAS, 414, 1667

Hora J. L., Latter W. B., Smith H. A., Marengo M., 2006, ApJ, 652, L426

Huggins P. J., Mauron N., 2002, A&A, 393, 273

Jacoby G. H., Ferland G. J., Korista K. T., 2001, ApJ, 560, L272

Lindegren L., et al., 2021, A&A, 649, 4

Liu X. W., et al., 2001, MNRAS, 323, 343

Liu Y., Liu X. W., Barlow M. J., Luo S. G., 2004, MNRAS, 353, 1251

Manchado A., Stanghellini L., Villaver E., García-Segura G., Shaw R. A., García-Hernández D. A., 2015, ApJ, 808, L115

Martin T. B., Prunet S., Drissen L., 2016, MNRAS, 463, 4223

Matsuura M., et al., 2007, MNRAS, 382, 1447

Matsuura M., et al., 2009, ApJ, 700, L1067

McDonald I., van Loon J. T., Decin L., Boyer M. L., Dupree A. K., Evans A., Gehrz R. D., Woodward C. E., 2009, MNRAS, 394, 831

McDonald I., Zijlstra A. A., Boyer M. L., 2012, MNRAS, 427, 343

McDonald I., Zijlstra A. A., Watson R. A., 2017, MNRAS, 471, 770

Meixner M., McCullough P., Hartman J., Son M., Speck A., 2005, AJ, 130, 1784

Merchan-Benitez P., Uttenthaler S., Jurado-Vargas M., 2023, A&A, 672, 165

Miller Bertolami M. M., 2016, A&A, 588, 25

Miranda L. F., Torrelles J. M., Guerrero M. A., Vázquez R., Gómez Y., 2001, MNRAS, 321, 487

O'Dell C. R., McCullough P. R., Meixner M., 2004, AJ, 128, 2339

O'Dell C. R., Sabbadin F., Henney W. J., 2007, AJ, 134, 1679

O'Dell C. R., Ferland G. J., Henney W. J., Peimbert M., 2013a, AJ, 145, 92

O'Dell C. R., Ferland G. J., Henney W. J., Peimbert M., 2013b, AJ, 145, 170

Perrin M. D., Sivaramakrishnan A., Lajoie C.-P., Elliott E., Pueyo L., Ravindranath S., Albert L., 2014, in Oschmann Jacobus M. J., Clampin M., Fazio G. G., MacEwen H. A., eds, Society of Photo-Optical Instrumentation Engineers (SPIE) Conference Series Vol. 9143, Space Telescopes and Instrumentation 2014: Optical, Infrared, and Millimeter Wave. p. 91433X

Pontoppidan K. M., et al., 2022, ApJ, 936, L14

Rieke M. J. et al., 2023, PASP, 135, 028001

Sahai R., et al., 1998, ApJ, 493, L301

Sahai R., Morris M. R., Werner M. W., Güsten R., Wiesemeyer H., Sandell G., 2012, A&A, 542, 20

Simis Y. J. W., Icke V., Dominik C., 2001, A&A, 371, 205

Skrutskie M. F., et al., 2006, AJ, 131, 1163

Speck A. K., Meixner M., Jacoby G. H., Knezek P. M., 2003, PASP, 115, 170

Ueta T., Otsuka M., 2021, PASP, 133, 093002

van Hoof P. A. M., et al., 2010, A&A, 518, 137

Vassiliadis E., Wood P. R., 1994, ApJS, 92, 125

Vishniac E. T., 1983, ApJ, 274, L152

Whitmore B. C., et al., 2016, AJ, 151, 134

Wright G. S. et al., 2023, PASP, 135, 048003

Zanstra H., 1955, Vistas in Astronomy, 1, 256

Zhang Y., Liu X. W., Wesson R., Storey P. J., Liu Y., Danziger I. J., 2004, MNRAS, 351, 935

Zijlstra A. A., Bedding T. R., 2002, JAAVSO, 31, 2

APPENDIX A: NIRCAM IMAGES

Fig. A1 shows NIRCam images with individual filter bands. The F162M image is distinctly different from the rest of NIRCam images, being bright in the ring, with little emission from halo. This filter contains continuum, presumably, free–free emission, and hydrogen recombination lines, and these are fainter than molecular hydrogen emission, which dominates the other three NIRCam images.
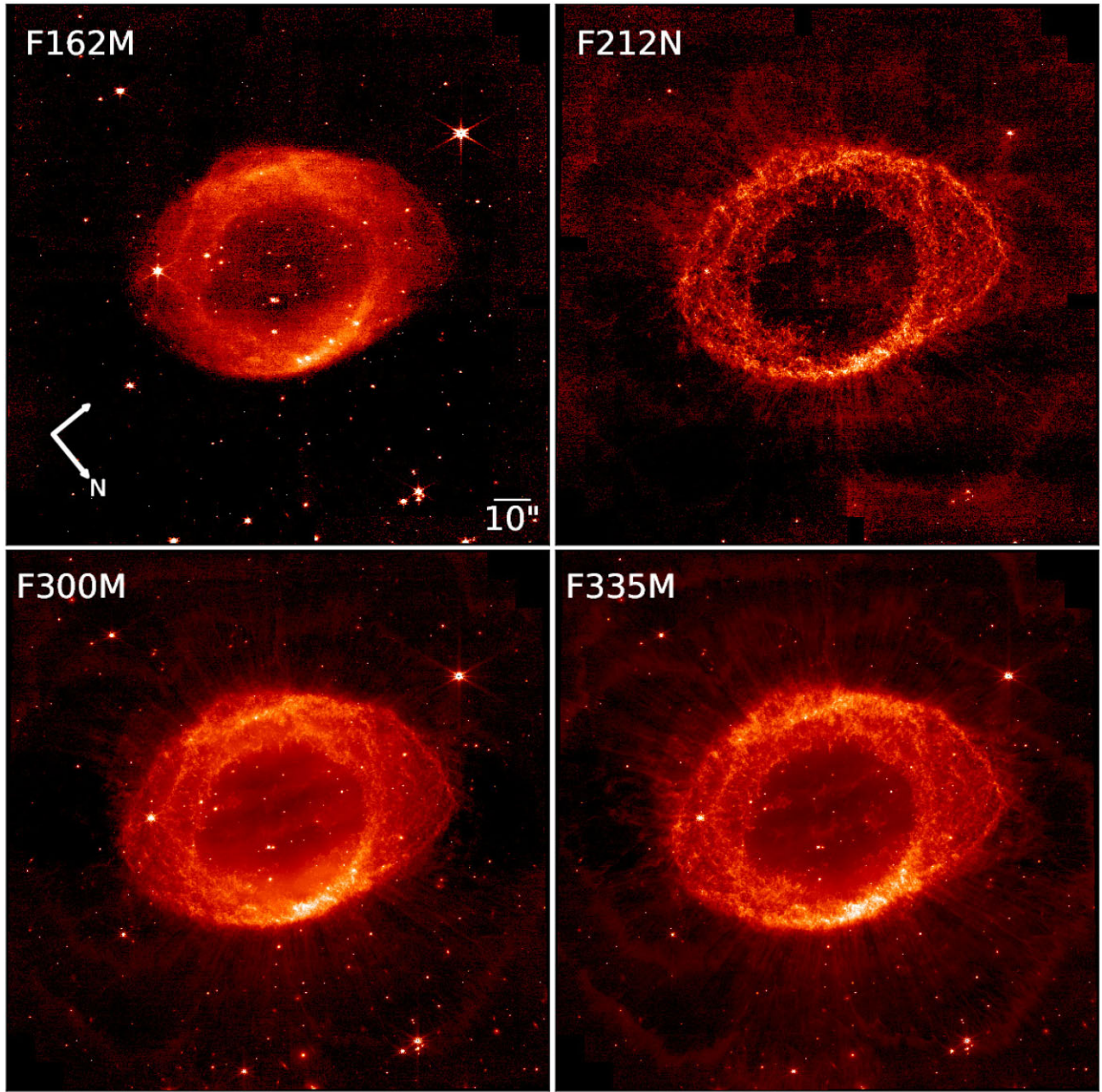
Figure A1. NIRCam individual images.
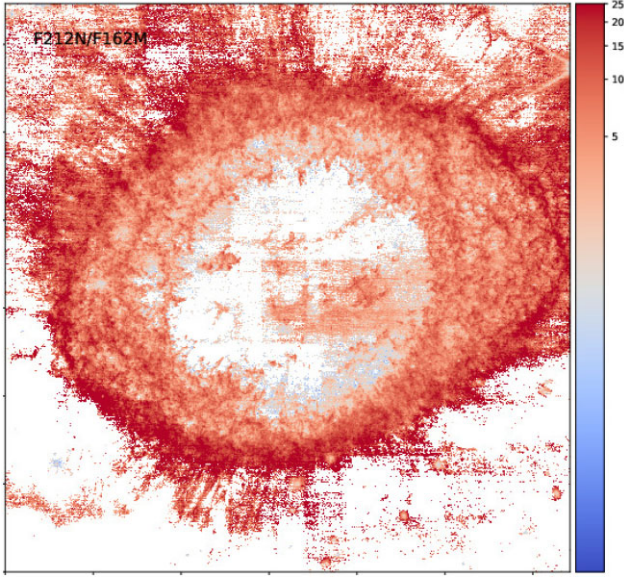
**Figure B1.** F212N/F162M ratio in log scale.

APPENDIX B: FLUX RATIO IMAGES

Figs B1–B3 show flux ratio images of pairs of filter bands, demonstrating the contributions of different lines/continuum or dust at different locations.

Fig. B1 demonstrates that H_2 emission is found in many globules, and across the halo. Due to its large dynamical range, this image only is plotted on log scale.

Fig. 11 shows the F335M/F300M image. Similar to Fig. B1, the F335M/F300M colour is reddest at the outer edge of the shell. These two filter bands contain more or less similar components (Table 1). This red edge at the shell may be explained by the additional contribution of PAHs to the emission in the F335M filter passband. If it is due to different H_2 line ratio, or continuum, the colour should be redder as further away from the central star, but that is not found in this figure. Hence, most likely PAHs are contributing to F335M at the edge of the shell, where UV radiation from the central star may fall onto the appropriate conditions for UV excitation.

Figs B2 and B3 show MIRI flux ratio images. MIRI F560W–G1130W images tend to have substantial contributions from the continuum, with additional line contributions on top. The F770W/F560W and F1130W/F770W images show similar colour patterns: the shell has rather similar colour within, in contrast to the F335M/F300M image. The F770W and F560W filters contain similar emission-line contributions, with additional Ar II emission in F770W. This additional Ar II contribution probably characterises the blue stripe structure inside the cavity, and the cavity itself. The edge of the shell is rather red in F770W/F560W, which may suggest a contribution from PAHs at this location. F1130W/F1000W looks very similar to F335M/F300M with the presence of red colour at the edge of the shell. Considering that F1130W has the least line contribution amongst all filter bands, having the reddest colour at the shell edge could be due to PAHs, while the red colour in the halo might be due to the contribution from cold dust emission (Cox et al. 2016).
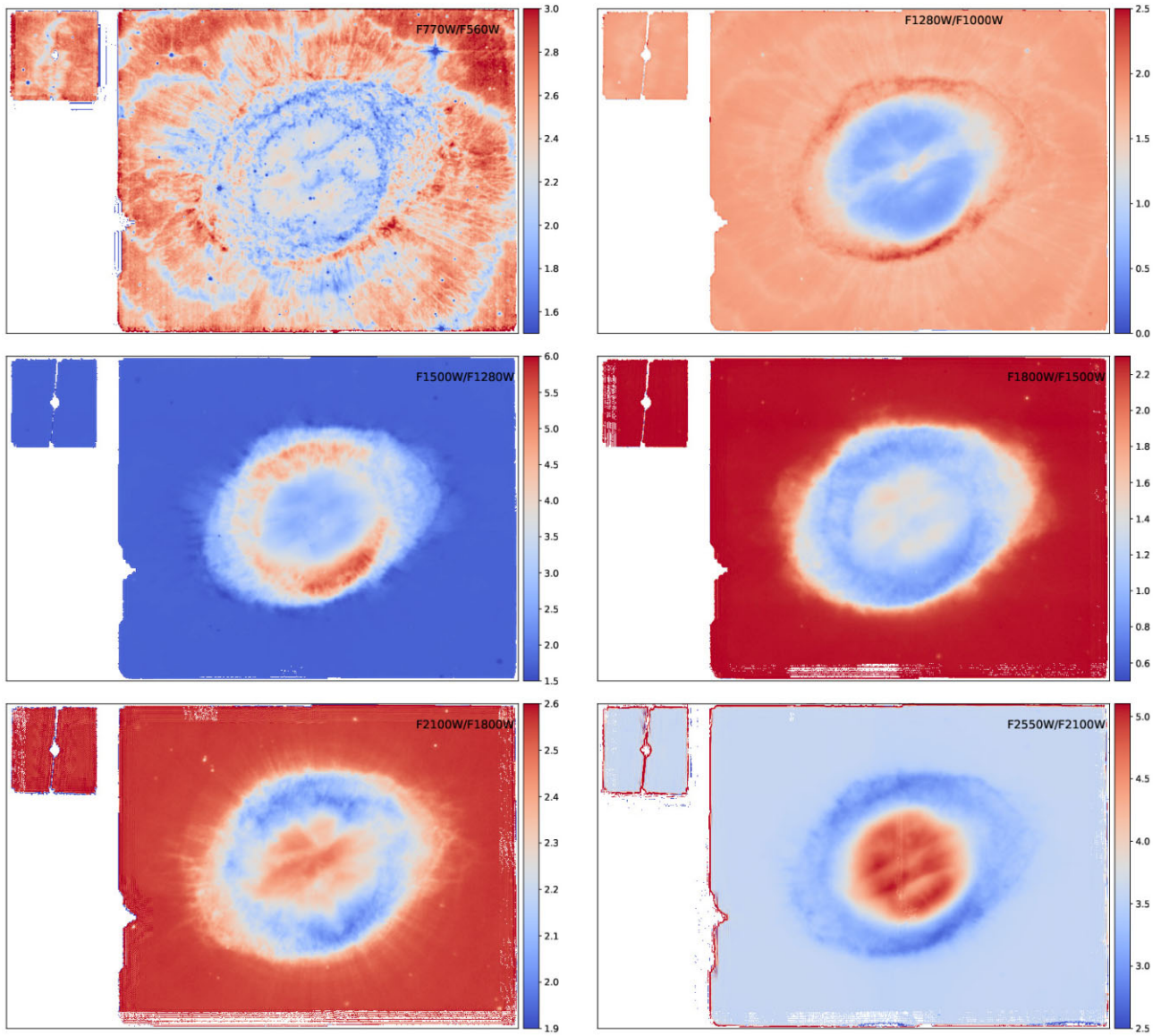
Figure B2. MIRI colour (flux ratio) images.
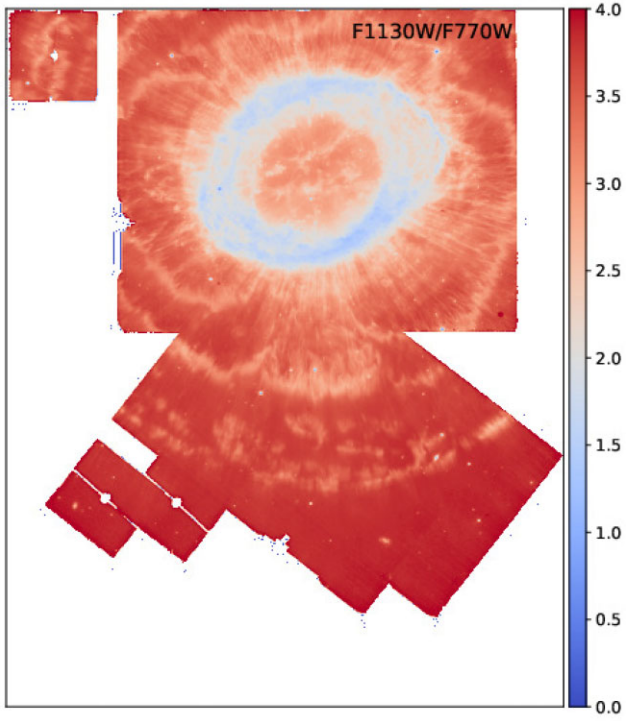
Figure B3. MIRI colour of F1130W/F770W, which includes the extension towards the north-west.
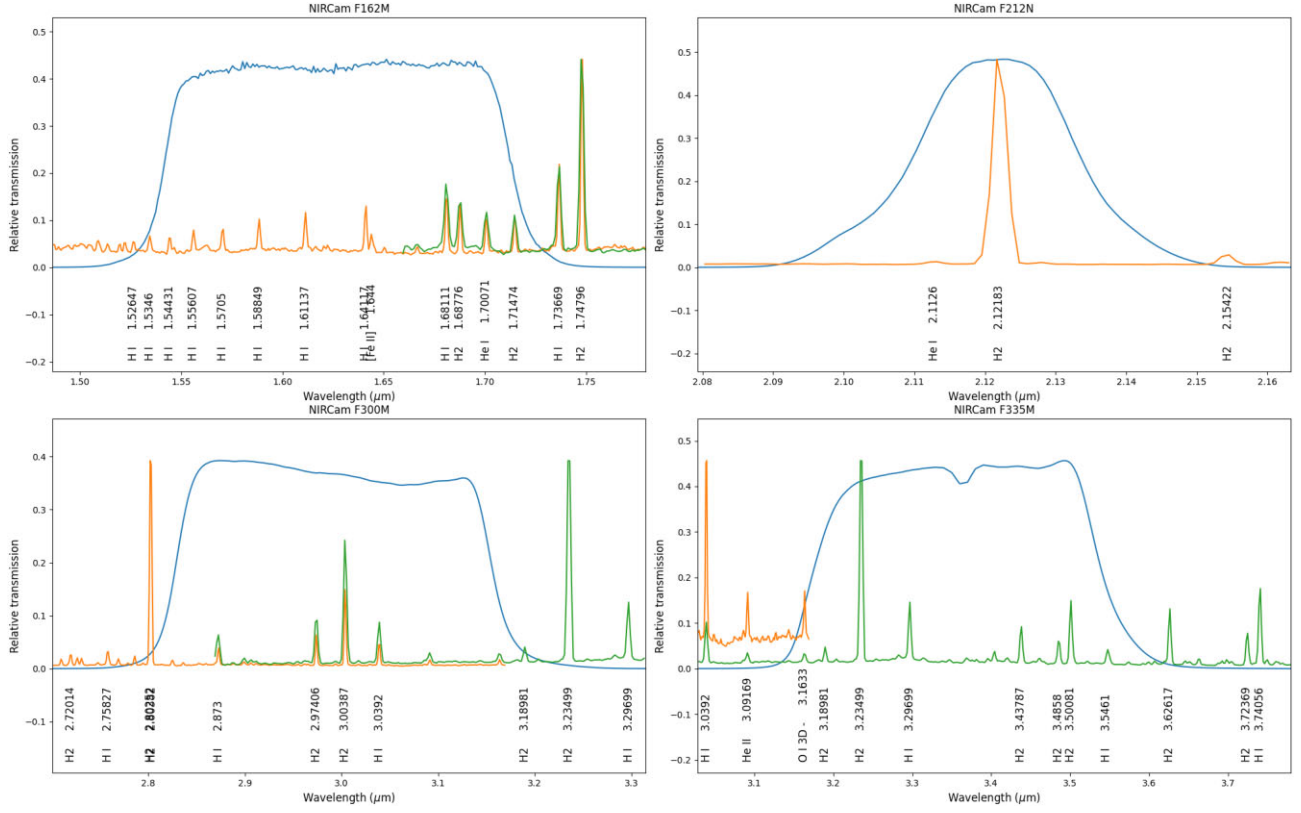
APPENDIX C: FILTER TRANSMISSION CURVES

Figs C1 show the filter transmission curves [8][9] overlaid with NIRSpec and MIRI MRS spectra of the north region.

[8]https://jwst-docs.stsci.edu/jwst-near-infrared-camera/nircam-instrumentation/nircam-filters
[9]https://jwst-docs.stsci.edu/jwst-mid-infrared-instrument/miri-instrumentation/miri-filters-and-dispersers

Figure C1. The NIRCam filter transmission curves with NIRSpec spectra from the Northern part of the Ring. Line identifications from van Hoof et al. (in preparation) are included.
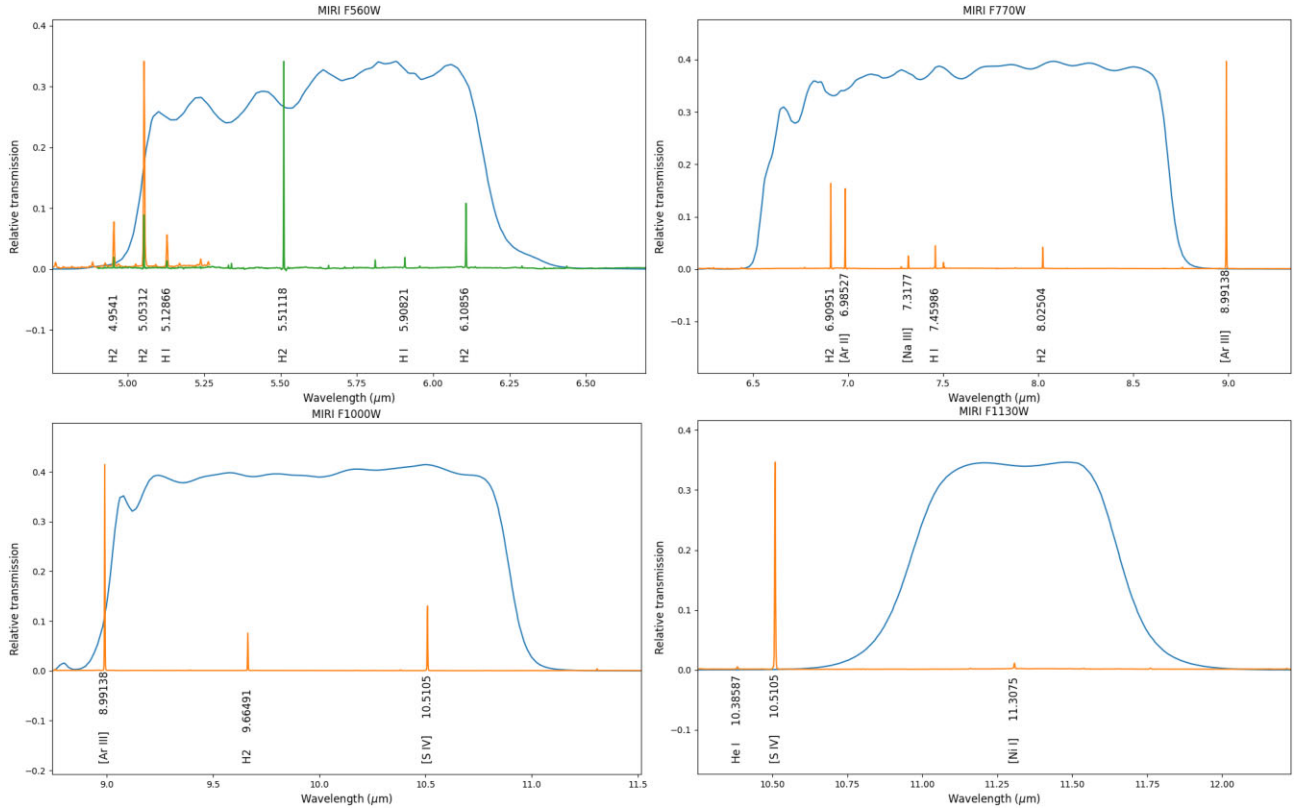
Figure C2. The same as Fig. C1, but MIRI filters with MIRI MRS spectra.
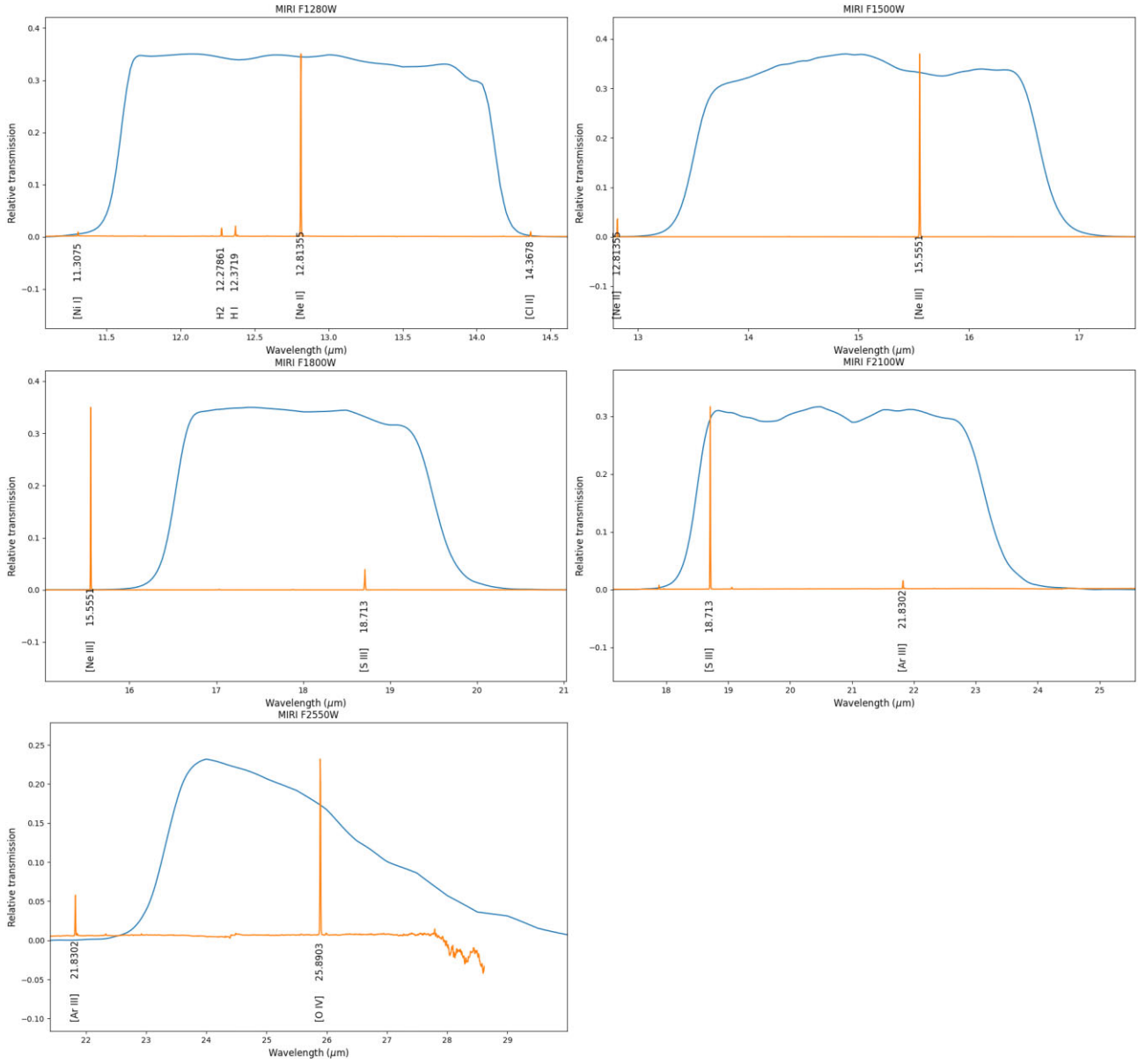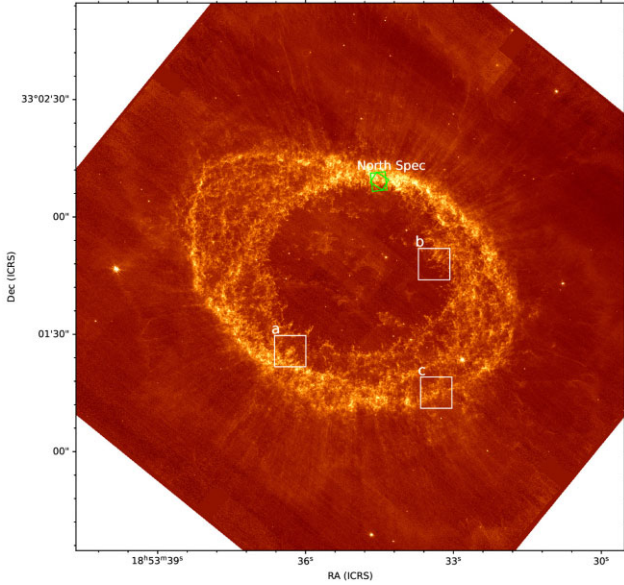
Figure C2. Continued.

Figure C3. Locations of globules plotted in Fig. 7 indicated by white boxes. The green boxes show the region where the northern spectra were taken. These spectra were used for filter transmission curves (Figs C1 and C2) and contributions of lines into the filters Table 1. The smaller green box is for NIRSpec and the larger green box is for MIRI/MRS, both representing the smallest FoVs (fields of view) of these two instruments, as their FoVs have wavelength dependence.
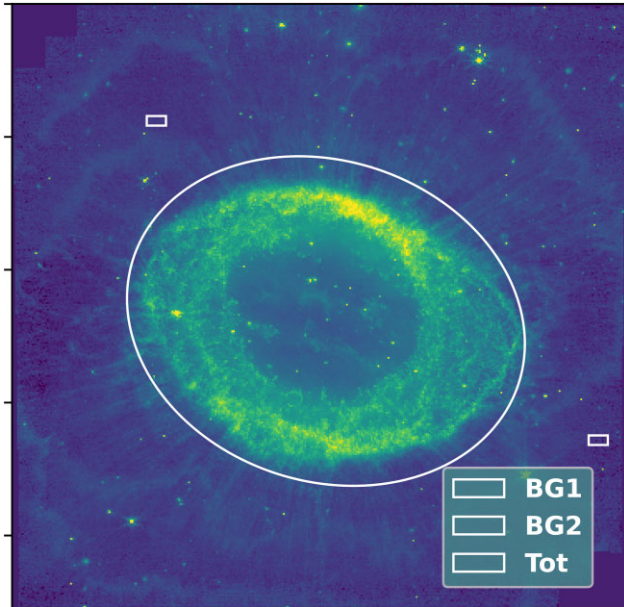
Figure C4. Image showing the area used for the flux density (Tot) and the background regions (BG1 and BG2). The orientation is the same as Fig. 1.

[1]*Cardiff Hub for Astrophysics Research and Technology (CHART), School of Physics and Astronomy, Cardiff University, The Parade, Cardiff CF24 3AA, UK*
[2]*Department of Physics and Astronomy, University College London, Gower Street, London WC1E 6BT, UK*
[3]*Department of Physics & Astronomy, Jodrell Bank Centre for Astrophysics, The University of Manchester, Oxford Road, Manchester M13 9PL, UK*
[4]*Space Telescope Science Institute, 3700 San Martin Drive, Baltimore, MD 21218, USA*
[5]*Department of Experimental Physics, Maynooth University, Maynooth, Co Kildare, Ireland*
[6]*School of Cosmic Physics, Dublin Institute for Advanced Studies, 31 Fitzwilliam Place, Dublin 2, Ireland*
[7]*Instituto de Astronomía, Universidad Nacional Autónoma de México, 22860 Ensenada, B.C., Mexico*
[8]*Department of Physical Sciences, The Open University, Walton Hall, Milton Keynes, MK7 6AA, UK*
[9]*Jet Propulsion Laboratory, California Institute of Technology, Pasadena, CA 91011, USA*
[10]*ACRI-ST, Centred'Etudes et de Recherche de Grasse (CERGA), 10 Av. Nicolas Copernic, F-06130 Grasse, France*
[11]*INCLASS Common Laboratory, 10 Av. Nicolas Copernic, F-06130 Grasse, France*
[12]*Department of Computer Science, Institute of Mathematics and Statistics, University of São Paulo, Rua do Matão 1226, Cidade Universitária, 05508-090 São Paulo, SP, Brazil*
[13]*Instituto de Física e Química, Universidade Federal de Itajubá, Av. BPS 1303, Pinheirinho, 37500-903 Itajubá, MG, Brazil*
[14]*Department of Physics and Astronomy, University of Western Ontario, London, ON N6G 2V4, Canada*
[15]*Institute for Earth and Space Exploration, University of Western Ontario, London, ON N6A 3K7, Canada*
[16]*SETI Institute, Mountain View, CA 94043, USA*
[17]*University of Texas at Austin, Austin, TX 78712, USA*
[18]*Chalmers University of Technology, Onsala Space Observatory, SE-439 92 Onsala, Sweden*
[19]*Instituto de Astrofísica de Canarias, E-38205 La Laguna, Tenerife, Spain*
[20]*Departamento de Astrofísica, Universidad de La Laguna, E-38206 La Laguna, Tenerife, Spain*
[21]*Consejo Superior de Investigaciones Científicas (CSIC), E-28014 Madrid, Spain*
[22]*Royal Observatory of Belgium, Ringlaan 3, B-1180 Brussels, Belgium*

This paper has been typeset from a TEX/LATEX file prepared by the author.